Journal of Structural Geology 204 (2026) 105623

Contents lists available at ScienceDirect

Journal of Structural Geology

journal homepage: www.elsevier.com/locate/jsg

Rift development at the Askja Fissure Swarm, Iceland

Fabio Luca Bonali [a,b,*], Martina Pedicini [a], Thomas R. Walter [c], Alessandro Tibaldi [a,b]

[a] Department of Earth and Environmental Sciences, University of Milan-Bicocca, 20126, Milan, Italy
[b] CRUST-Interuniversity Center for 3D Seismotectonics with Territorial Applications, 66100, Chieti Scalo, Italy
[c] GFZ Helmholtz Centre for Geosciences, Telegrafenberg, 14473, Potsdam, Germany

ARTICLE INFO

Keywords:
Holocene normal faults
Askja rift
Iceland
Fault propagation
Extension fractures
Dykes

ABSTRACT

Understanding how faulting and dyke intrusion interact to control rift development in volcanotectonic systems remains a key challenge, particularly in areas where multiple magma sources coexist. Here, we contribute to this topic by providing a high-resolution structural dataset for the Askja Fissure Swarm (AFS), one of the major rifts of the Northern Volcanic Zone of Iceland (NVZ), where central volcanoes and their associated dyke-fissure swarms act as magma plumbing systems and long-term eruption sources. We describe the Holocene structures of the AFS through the analysis of high-resolution remote sensing data and virtual field reconnaissance. We developed an inventory of 3749 individual structures, including dykes and fractures, mapped at a scale of 1:50,000, and systematically measured their strike, dip direction, length and kinematics. We recognized 395 eruptive fissures, 2301 extension dry fractures (fissures), and 1038 normal faults, of which 536 dip eastward and 502 westward. Along the main faults, we reconstructed the slip profiles, with the aim of evaluating the direction of along-axis fault and rift propagation. The overall dataset exhibits a predominant N–S to NNE–SSW strike, with an average strike of N17.5°E. Structure lengths vary from 10 m up to 13 km, with a mean of 445 m. Normal faults are generally longer than other structures, with a mean of 1042 m. With distance to the central volcanoes, we find the number of extension fractures and faults, their lengths and the slip profiles decrease. We interpret these characteristics as the effect of multiple dykes that laterally propagated outward from the magma chambers below Askja and Hrúthálsar central volcanoes. We also observed variation of fracture intensity and strike where the AFS intersects possibly hidden inherited transversal structures. Looking at the whole AFS, the tapering of fault slip profiles shows a dominant northward propagation of faults. This may indicate the superimposition of a regional northward propagation of the rift on the local effects of dykes and magma chambers, consistent with the northward spread of the NVZ.

1. Introduction

Iceland presents a rare opportunity to directly investigate the architecture and dynamics of divergent plate boundaries characteristic for mid-ocean ridges, as it is one of the few locations worldwide where such an active boundary is exposed above sea level. This exposure is attributed to the high volumes of lava production and uplift associated with the Icelandic hotspot (Einarsson, 1991). The structure of a plate boundary can be reconstructed by deciphering the geometry and kinematics of the various structures such as faults, extensional dry fractures, and eruptive fissures. A more complete understanding of such a boundary can be derived also by the reconstruction of the rift propagation. Whereas the literature on geometry and kinematics of divergent plate boundaries is extremely rich and detailed, rift propagation has been most studied by a regional approach. Numerical modelling has played a key role in exploring rift propagation from a broader regional perspective, as reported in Parmentier and Schubert (1989), Van Wijk and Blackman (2005), Koehn et al. (2008), and Koopmann et al. (2014). Along similar lines, analogue modelling has been utilized to study rift propagation (e.g. McClay and White, 1995; Mart and Dauteuil, 2000; Corti et al., 2003; Zwaan et al., 2020). In the Icelandic context, the works of Cooper et al. (1987), Jacques et al. (1999), and Keir et al. (2006) analyse the distribution of earthquakes with the aim of gaining a better understanding of the tectonics and rifting processes associated with the interaction between the Mid-Atlantic Ridge and the Icelandic crust. And of course, also offshore rift propagation studies have a regional focus driven by the intrinsic nature of oceanographic surveys and the difficult environment (Schouten et al., 1987; Carbotte et al., 1991; Wilson and

* Corresponding author. Department of Earth and Environmental Sciences, University of Milan-Bicocca, 20126, Milan, Italy.
E-mail address: fabio.bonali@unimib.it (F.L. Bonali).

https://doi.org/10.1016/j.jsg.2026.105623
Received 17 September 2025; Received in revised form 2 January 2026; Accepted 5 January 2026
Available online 10 January 2026

Hey, 1995; Tibaldi et al., 2008; Franke et al., 2015). Recent studies on the rifting events at Krafla (1975-1984), Holuhraun (2014-2015) and Fagradallsfjall (2021) underline that pre-existing and long-established structures and faults play an important role in unrest episodes, and that the fissures, faults, and fractures are complexly activated in oblique rifting segments (Ágústsdóttir et al., 2016; Tibaldi et al., 2020; Døssing et al., 2024).

Detailed studies on rift propagation have been recently developed through field surveys and analogue modelling (Schlagenhauf et al., 2008; Zwaan et al., 2020), including slip profiles along rifts (Tibaldi et al., 2019, 2020a, 2020b, 2020c; Pedicini et al., 2023, 2025). These slip profiles, or displacement-length profiles, quantify the height of the fault scarp as a function of distance along the fault trace. They serve as a proxy for recording the cumulative displacement resulting from various stages of fault growth (Schlagenhauf et al., 2008). A fault that grows symmetrically by extending vertically and at both tips, is characterised by an elliptic fault slip profile, with the center of the fault showing the greatest slip (Pollard and Segall, 1987; Cowie and Scholz, 1992; Scholz, 2002). Instead, a fault can grow asymmetrically with an increase of the fault scarp height towards one tip, and unidirectional propagation of the fault towards the opposite tip (Manighetti et al., 2001). This produces an asymmetric shape of the fault slip profile, as observed worldwide (Peacock and Sanderson, 1991; Bürgmann et al., 1994; Nicol et al., 1996; Manighetti et al., 2001, 2004; Roche et al., 2012; Dumont et al., 2017; Tibaldi et al., 2019, 2020b; Macheyeki and Macheyeki, 2025). Moreover, Rotevatn et al. (2019) shows that normal fault growth commonly reflects the combined effects of segment linkage and fault tip propagation, producing complex displacement–length relationships that preserve the structural memory of fault evolution. The reconstruction and analysis of the slip profile of all the (identifiable) faults that compose a rift, can give detailed clues on the general and local pattern of propagation of a divergent plate boundary.

In Iceland, the Northern Volcanic Zone (NVZ) represents the onshore prolongation of the Middle Atlantic Ridge. The NVZ is one of Iceland's most active volcanic rift systems, where deformation events, seismicity and volcanic eruptions frequently occur. It is composed of seven N-S- to NNE-SSW-trending volcanotectonic systems (or fissure swarms) named, from west to east: Tungnafellsjokull, Theistareykir, Krafla, Bardarbunga, Fremrinamar, Askja, and Kverkfjoll (Fig. 1) (Sæmundsson, 1979; Gudmundsson, 2000; Sigmundsson et al., 2020). After a general

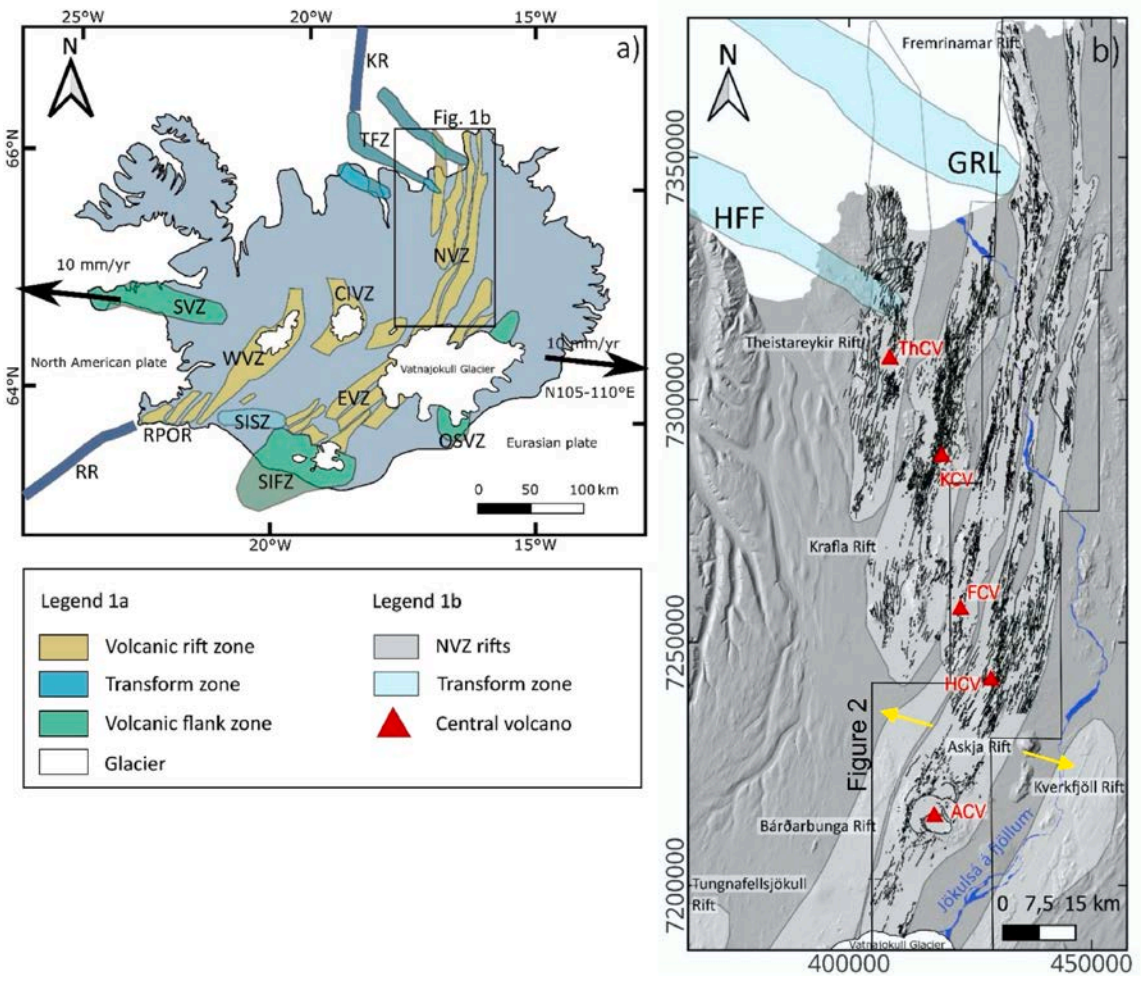

Fig. 1. Volcanotectonic framework of Iceland and the Northern Volcanic Zone (NVZ). (a) Map of Icelandic rifts and transform zones (modified after Einarsson and Brandsdottir, 1980; Hjartardóttir et al., 2016a; Sigmundsson et al., 2020). CIVZ, Central Iceland Volcanic Zone; EVZ, Eastern Volcanic Zone; NVZ, Northern Volcanic Zone; OSVZ, Öræfajökull-Snæfell Volcanic Zone; RPOR, Reykjanes Peninsula Oblique Rift; SIFZ, South Iceland Volcanic Flank Zone; SISZ, South Iceland Seismic Zone; SVZ, Snæfellsnes Volcanic Zone; TFZ, Tjörnes Fracture Zone; WVZ, Western Volcanic Zone. KR, Kölbeinsey Ridge; RR, Reykjanes Ridge. The black rectangle shows the location of Fig. 1b. (b) Detail of the NVZ with the studied area of Fig. 2; transform zones (in pale blue) and central volcanoes (red triangles) are reported. ACV, Askja Central Volcano; FCV, Fremrinamar Central Volcano; GRL, Grímsey Lineament; HCV, Hrúthálsar Central Volcano; HFF, Húsavík-Flatey Fault; KCV, Krafla Central Volcano; ThCV, Theistareykir Central Volcano. Black lines are late Quaternary fractures from Tibaldi et al. (2020a), Pedicini et al. (2023, 2025), Corti et al. (2021), and original data from the present work for the Askja Fissure Swarm. The ArcticDEM v.4.1 (Porter et al., 2023) is used as background. Yellow arrows indicate the spreading direction in the NVZ. (For interpretation of the references to colour in this figure legend, the reader is referred to the Web version of this article.)

reconstruction of the NVZ's structures' geometry by Hjartardóttir et al. (2016a), detailed analyses of the propagation of some of these volcanotectonic systems have been carried out by Bonali et al. (2019b), Tibaldi et al. (2019, 2020a, 2020b), Corti et al. (2021), and Pedicini et al. (2023, 2025), focusing on the Theistareykir, Krafla, and Fremrinamar fissure swarms.

In order to provide a large-scale and comprehensive analysis of the NVZ, here we present the inventory of all the structures of the Askja Fissure Swarm (AFS), including a distinction between faults and dry extensional fractures, which has not been done before. As part of our investigation, we produced a 1:50,000 scale structural map, which improves upon existing standards ranging from 1:250,000 to 1:100,000 (Sæmundsson, 1977; Sæmundsson et al., 2012; Sigurgeirsson et al., 2015), enabling a more precise structural interpretation. Besides, since our mapping covers the whole AFS, it extends previous local surveys such as the one of the Fjallagj graben by Tentler and Mazzoli (2005) and of the four areas of Panza et al. (2024). The studied area is particularly suitable for this type of study due to the lack of vegetation and glacial deposits, and the absence of alteration due to the very young age of the fractured deposits. Specifically, the higher-resolution structural mapping allows us to resolve the spatial distribution, kinematics, and along-axis propagation of faults, extensional fractures and eruptive fissures, and to quantitatively link surface deformation patterns to dyke intrusion and magma chamber activity along the AFS.

Based on the new inventory of thousands of structures, our study allowed to: *i)* better understand the structure, kinematics and propagation of the AFS, which is the longest rift (120 km) of the NVZ, *ii)* analyse the processes that guide deformation, and *iii)* evaluate AFS dynamic respect to the other volcanotectonic systems that compose the whole NVZ. Although these systems display varying individual characteristics, including length, geographical position, number of central volcanoes, and interaction with adjacent transform faults, a set of recurring structural features suggests shared deformation mechanisms. A nuanced understanding of volcanotectonic rifting processes not only enhances theoretical models but also aids in assessing seismic and volcanic hazards, as exemplified by recent unrest on the Reykjanes Peninsula (Ducrocq et al., 2024; De Pascale et al., 2024).

2. Geological background

2.1. General framework

Iceland is situated at the junction between the slow-spreading Mid-Atlantic Ridge (<20 mm/yr) and a deep-seated mantle plume, whose persistent magmatic activity has led to substantial crustal growth and thickening (Wilson, 1963; Morgan, 1972; Gudmundsson, 2000). The interaction between these two systems produces a complex plate boundary characterised by rift propagation, magmatic segmentation, and episodic rift jumps (Einarsson, 1991a; Sigmundsson et al., 2020). The relative motion between the North American and Eurasian plates in Iceland is approximately WNW–ESE, and within the active rift zones, including the NVZ, the local spreading direction is nearly orthogonal to the rift axis, oriented roughly N104°E to N110°E (e.g., Árnadóttir et al., 2009; Metzger and Jonsson, 2014; Corti et al., 2021). This extension direction plays a key role in controlling the orientation and kinematics of faults, fissures, and intrusions throughout the neovolcanic zones. Within this framework, the NVZ marks the northernmost segment of Iceland's active rift system. It accommodates a significant portion of the plate divergence through a series of NNE–SSW to N–S trending volcanotectonic systems, each composed of a central volcano and an associated fissure swarm (Sæmundsson, 1974; Einarsson, 2008) (Fig. 1). Among these, the AFS is of particular interest due to its well-developed structures and recent tectono-magmatic activity, making it an ideal case study for understanding the interplay between faulting, dyke propagation, and surface deformation.

2.2. The Askja Fissure Swarm

Located east of the Fremrinámar Fissure Swarm, the AFS extends for approximately 120 km from the northern margin of the Vatnajökull Glacier towards the north coast of Iceland (Sæmundsson, 1974; Einarsson and Brandsdóttir, 2021) (Fig. 1). The deposits cropping out along the AFS are essentially made of igneous rocks. The older deposits of Miocene, Pliocene and Pleistocene age mainly crop out in the northern part of the study area, whereas they become younger southward. In the central and southern part of the AFS, mostly outcrops are made of lavas emplaced after the Late Glacial Maximum (LGM), mostly belonging to the Odaðahraun alkaline lava field, dated younger than 10 ka and generally older than 1100 years (Sigurgeirsson et al., 2015; Hjartarson and Sæmundsson, 2014; Sæmundsson et al., 2012). At the latitude of 7245000, there is the Hrúthálsar Central Volcano (Figs. 2 and 3; Sæmundsson, 1974; Sæmundsson et al., 2005; Hjartardóttir and Einarsson, 2015). Here, lava deposits range from 10 to 7 ka BP, followed by lava units older than 7 ka BP, and finally by historical products, which mantle the pre-LGM deposits.

The southern part of the system hosts the Askja Central Volcano, active since at least 200–300 ka (Brown et al., 1991; Sigvaldason, 2002). The volcanic edifice comprises both subglacial and interglacial basaltic deposits and features three calderas, the youngest of which formed during the major volcanotectonic event of 1874–1876 AD (Sigurdsson and Sparks, 1978; Sturkell and Sigmundsson, 2000; Hartley and Thordarson, 2012). This episode also reactivated the fissure swarm, producing an eruption at the Sveinagjá Graben. Although initially attributed to a dyke originating from Askja Central Volcano, later petrological and geochemical studies indicate a more complex magmatic plumbing system (Macdonald et al., 1987; Hartley and Thordarson, 2013).

The fissure swarm includes numerous normal faults, extension dry fractures, and eruptive fissures aligned with the regional stress field. While non-eruptive fractures are more common in the distal parts of the swarm, eruptive fissures tend to be concentrated within 20–30 km of the central volcano (Hjartardóttir et al., 2016b). Most structures strike NNE, consistent with the regional extension direction, although deviations occur near the caldera and in structurally complex areas.

The most recent eruptions occurred in 1921–1929 and in 1961, and the most recent episodes of major rifting occurred in 1874–1876 and in 2014–2015, when magma from Bárðarbunga propagated laterally for approximately 45 km before erupting within the ASF (Sigmundsson et al., 2015; Gudmundsson et al., 2016). This event triggered graben subsidence, formation of new surface fractures, and the reactivation of older eruptive features (Hjartardóttir et al., 2016a).

3. Methodology

3.1. Photogrammetry processing of aerial photos

We primarily employed orthomosaics and Digital Surface Models (DSMs) derived from historical aerial imagery. The aerial photographs sourced from the National Land Survey of Iceland (https://www.lmi.is/), had a photogrammetric overlap and sidelap, and hence could be processed using Agisoft Metashape v.2.1.1 (https://www.agisoft.com/), a Structure-from-Motion (SfM) software that reconstructs three-dimensional features from overlapping images (Stal et al., 2012; Westoby et al., 2012; Schönberger and Frahm, 2016; Bonali et al., 2019a). For the study of the Askja rift, a set of 221 aerial photographs, captured in 1987 by the National Land Survey of Iceland, was processed. These images were acquired at a flight altitude of approx. 6000 m a.s.l., with 60 % longitudinal overlap and a focal length of 151.78 mm. Processing followed the same methodology as outlined in Pedicini et al. (2023, 2025); water bodies and image edges were masked to improve reconstruction. Photo alignment was performed using medium accuracy to generate a sparse point cloud, followed by the generation of a dense

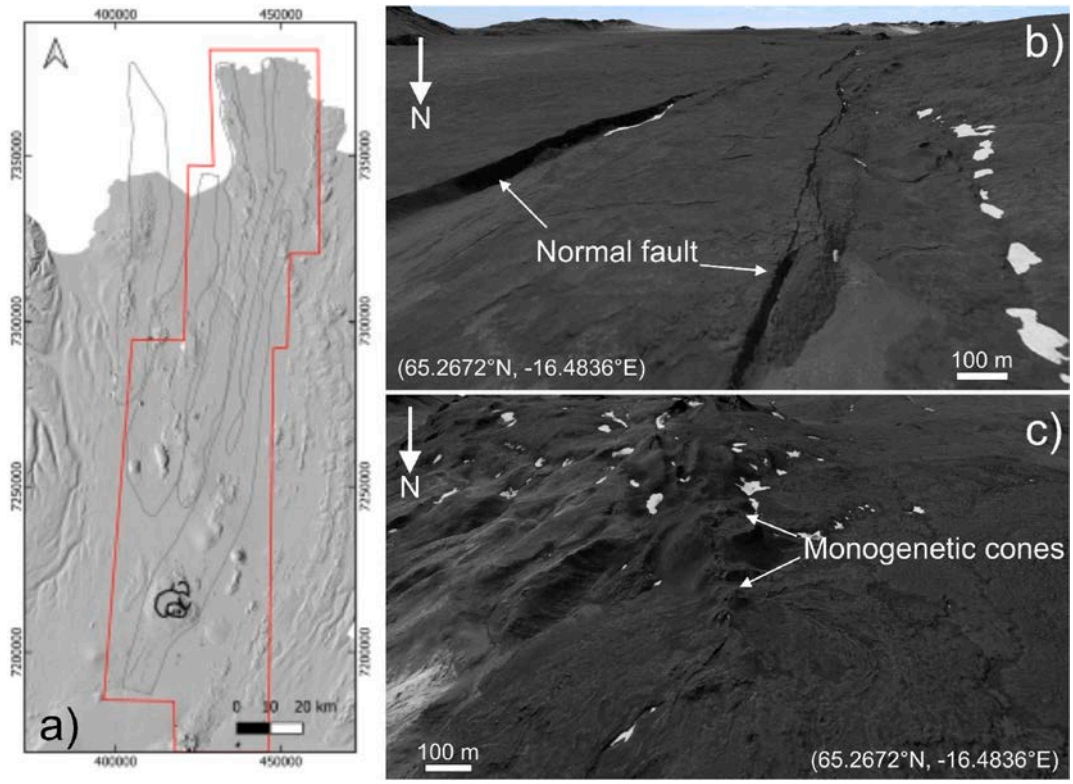

Fig. 2. (a) Map showing the areal coverage of the photogrammetry-derived 3D models of the Fremrinámar and Askja fissure swarms, Fremrinámar area has been studied by Pedicini et al. (2023); ArcticDEM v.4.1 (Porter at el., 2023) is used as a background. Black lines outline the Askja caldera. Key examples of virtual field checks carried out in the present work to carefully identify (b) normal faults and (c) eruptive fissures inferred from monogenetic cone alignments.

point cloud with a medium-quality setting. As the aerial photographs were not geotagged, our workflow included the extensive use of ground control points (GCPs). In our case, as no GCPs were physically placed during the acquisition of the aerial photographs, GCPs were retrospectively defined using stable, clearly recognizable features (e.g., lava flow edges, road intersections, and large boulders) identifiable in both the historical imagery and modern georeferenced datasets, from which their X–Y coordinates were extracted; Z values were obtained from elevation control points derived from available topographic maps provided by the National Land Survey of Iceland.

A total of 90 GCPs were used for georeferencing, resulting in a fully referenced orthomosaic with 0.54 m/pixel resolution and a digital surface model (DSM) with 2.15 m/pixel resolution. The orthomosaics and DSMs were analysed within QGIS v.3.28.4, a freely available geoinformatics software package, to map all volcanotectonic features within the ASF; the validity of data collected on such models has been already carried out in two previous work (Pedicini et al., 2023, 2025). Where necessary (e.g. snow cover in aerial photographs), we also used high-resolution imagery from the Google Satellite WMS Layer and ArcticDEM v.4.1 (Porter et al., 2018, 2023). Due to the spatial continuity between the Fremrinámar and Askja fissure swarms, datasets produced for the Fremrinámar (Pedicini et al., 2023) were also utilized to cover the northern and central Askja sectors, as shown in Fig. 2a.

3.2. GIS mapping and classification

Structural mapping in geology involves the identification, interpretation, and representation of lineaments and geological structures like faults or fractures. Due to the heterogeneity of data and resolutions, instead of using automatic or semi-automatic methods (based on edge detection or Deep learning models), herein we perform digitization based on interpreting and capturing structural data by hand based on high resolution orthomosaics, DSMs, and derivatives thereof (slope maps, aspect maps, shaded relief maps). All fracture swarms were initially mapped at a scale of 1:5000 and later summarised and represented at 1:50,000 within a GIS platform (QGIS v. 3.28.4). This scale was selected to achieve a more detailed depiction of the study area compared to previous maps, typically produced at scales between 1:250,000 and 1:100,000 (Sæmundsson, 1977; Sæmundsson et al., 2012; Sigurgeirsson et al., 2015). The mapping scale was further guided by the principle that, when the ratio between half the strike length of a fractured segment and half the spacing between the midpoints of collinear segments approaches one, the segments function as a single fracture (Sneddon and Lowengrub, 1969; Gray, 1992; Gudmundsson, 2011). This method was applied to key areas, confirming that mapping at 1:50,000 yielded comparable results. Digitized structures were classified into three categories: *i)* eruptive fissures, *ii)* dry fissures (here referred to as extension fractures), and *iii)* normal faults. Normal faults were distinguished from extension fractures through the analysis of shaded DSMs and orthomosaics, and further classified according to eastward or westward dip. Eruptive fissures were identified *via* morphometric analysis of eruptive centers (Tibaldi, 1995; Tibaldi and Bonali, 2017) or based on proximity to lava flows emitted in the fissure zone.

Additionally, a series of Virtual Field Checks (e.g. Fig. 2b–c) has been carried out using Immersive Virtual Reality tools, named GeaVR (https://www.geavr.eu/), which help resolve ambiguities in the above classification thanks to the in-person and holistic approach enabled by the exploration of 3D models derived from photogrammetric processing (see the following paper for more details, Gerloni et al., 2018; Antoniou et al., 2020; Tibaldi et al., 2020; Harknett et al., 2022; Bonali et al., 2024a,b).

3.3. Quantitative analysis

A quantitative assessment was conducted by measuring the length, azimuth, and mean X and Y coordinates of each mapped structure. These

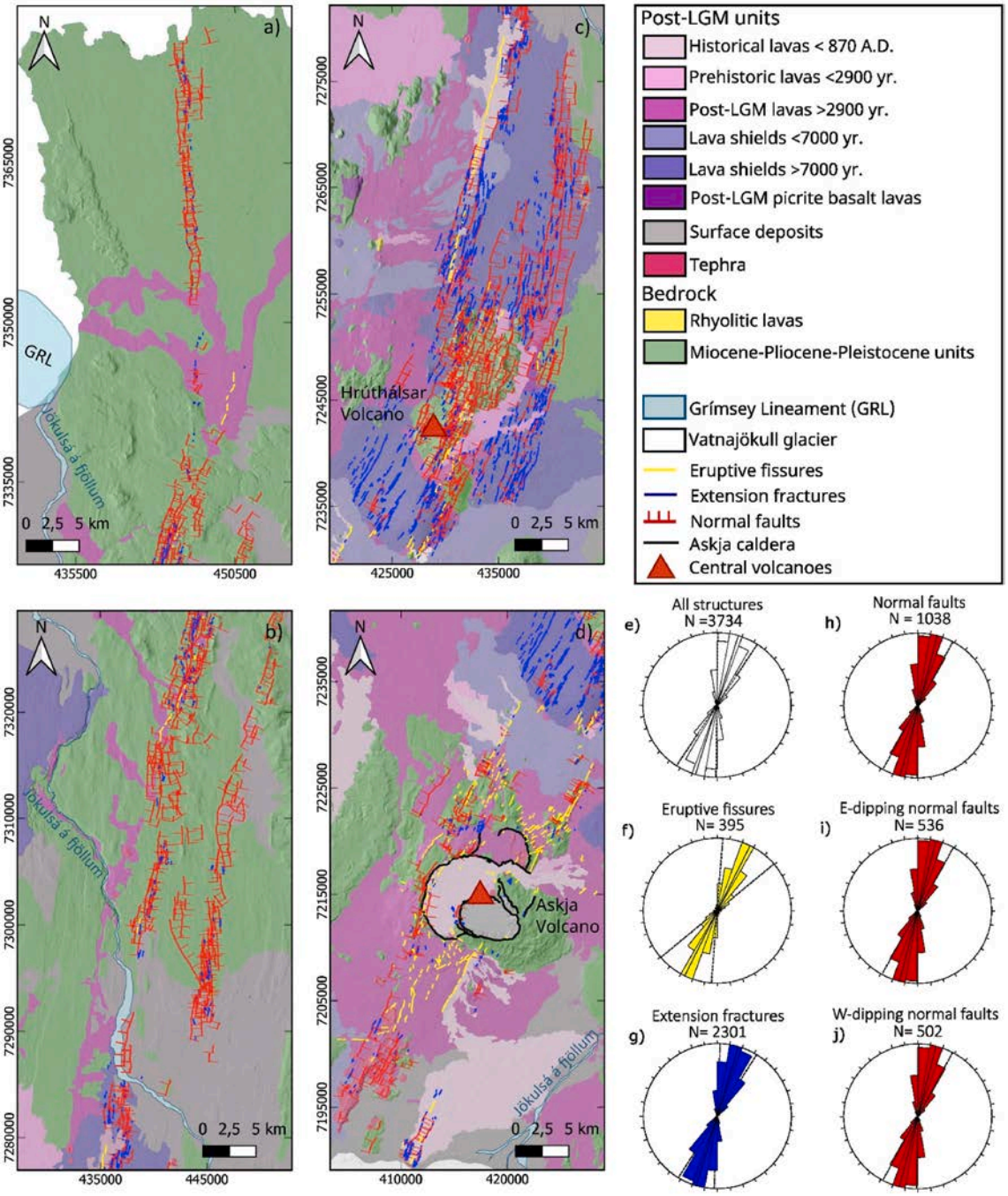

Fig. 3. *(a-d) Map of the AFS, whose structures are depicted via different colours. Geological units are modified after* Sæmundsson et al. (2012) and Sigurgeirsson et al. (2015). *The ArcticDEM v.4.1 (Porter at el., 2023) is used as a background. Location in* Fig. 1. *Rose diagrams represent the strike orientation of (e) the entire dataset, (f) eruptive fissures, (g) extension dry fractures, (h) normal faults, (i) E-dipping normal faults, and (j) W-dipping normal faults. Black solid and dashed solid lines represent each set's average strike and standard deviation, respectively.* (For interpretation of the references to colour in this figure legend, the reader is referred to the Web version of this article.)

parameters were then evaluated through scatterplot analysis to explore their spatial variation across the fissure swarm.

Vertical offsets within the AFS were determined using topographic profiles extracted mainly from photogrammetry-based DSMs and, where necessary, ArcticDEM v.4.1 (Porter et al., 2023). Elevation differences were measured between the tangents to the scarp crest and base, following the methodology of Hjartardóttir and Einarsson (2021).

A network of 382 transects striking N106°E and spaced at 500 m intervals was employed to quantify fracture frequency, rift width, and dilation across the rift. Dilation was estimated by calculating fault heave, assuming a subsurface fault dip of 75°, consistent with typical fault geometries of the Pleistocene–Holocene in Iceland (Forslund and Gudmundsson, 1991). This represents the minimum dilation since, for logistic reasons, it has not been possible to add the opening amount of the extension fractures.

Field validation of the measurements was feasible only in a very limited number of sites due to the remoteness of the area, they are manly located in the nearby of roads that cross structures. In any case, the methodology used here is the most efficient, even taking into account the vastness of the AFS (about 2400 km^2), and provides a robust

structural analysis of the entire region and all structures. Although remote sensing data may be subject to associated uncertainties, these are largely overcome by the robust statistical analysis based on thousands of data.

3.4. Fault slip profiles

To assess the along-strike deformation of normal faults within the ASF, slip (or displacement–length) profiles were generated for faults exceeding 2 km in length, following the methodology described by Manighetti et al. (2001) and Tibaldi et al. (2020a), who considered this fault length to be reliable for the robust detection of slip profiles. These profiles characterise how fault throw varies along the fault trace and are widely recognized as effective tools for reconstructing fault growth and propagation patterns (Schlagenhauf et al., 2008; Manighetti et al., 2004; Tibaldi et al., 2019, 2020c, 2025; Dumont et al., 2017).

Measurement points were established at arbitrarily chosen 200 m intervals along fault scarps within the AFS, the intervals providing sufficient spatial resolution for analysing the relevant structures. Throw values were extracted from high-resolution photogrammetry-derived digital surface models (DSMs) as well as from the ArcticDEM v.4.1 (Porter et al., 2023). Resulting slip profiles were categorised into four classes, consistent with the classification scheme adopted for other Iceland rifts: (i) symmetric, (ii) northward-tapering asymmetric, (iii) southward-tapering asymmetric, and (iv) unclassified. Although this analysis focuses solely on Askja, the reliability of the methodology has been independently validated through detailed field investigations in both the Krafla and Fremrinámar rifts (Pedicini et al., 2023; 2025). In these regions, 23 selected fault segments were surveyed to ground-truth the remote sensing interpretations, verify measurements of fracture length and orientation, and identify additional fault scarps with vertical offsets $\geq$1.0 m not resolved in DSM data. These field checks confirm the robustness and applicability of the slip profiling approach used in the AFS.

3.5. Validation and uncertainty

The robustness of the mapped structural dataset was assessed through multiple validation strategies. First, we performed cross-checks with existing geological maps of the NVZ (e.g., Sæmundsson et al., 2012; Sigurgeirsson et al., 2015), confirming consistency in both fault location and orientation in overlapping areas. Our mapping significantly increases resolution compared to previous maps (1:50,000 vs. 1:100,000 or coarser), yet maintains strong agreement in regional-scale structural patterns.

Secondly, where possible, we conducted field verification campaigns in selected accessible locations, particularly within the Fremrinámar and Krafla systems (see also Pedicini et al., 2023, 2025), using these observations as analogues to confirm the accuracy of DSM-derived fracture traces, vertical offsets, and fault dips in the present work. In those cases, structures identified through remote sensing were found to correspond to real fault scarps with vertical offsets exceeding 1 m. This confirms that the methodology used here can reliably detect and quantify rift-related structures, even in the absence of full field access. Additionally, in the present work, the virtual fracture classification was cross-validated using immersive 3D visualization (VR) of the photogrammetric models, allowing for an intuitive inspection of subtle scarps, strike changes, and fracture terminations (Gerloni et al., 2018; Antoniou et al., 2020, 2020b). This method proved particularly valuable for distinguishing between normal faults and dry extension fractures.

Uncertainty in slip measurements is primarily associated with the resolution of DSMs (2.15 m) and the geometry of fault scarps. However, comparison with ArcticDEM data and field-validated locations suggests that these uncertainties are minimal for structures with offsets >1 m. Additional sources of error include variable snow cover, vegetation shadows, or lighting conditions in aerial imagery, which were mitigated through masking and complementary use of Google Satellite and ArcticDEM basemaps. Overall, the integration of multi-resolution DEMs, orthophotos, field analogues, and virtual validation techniques ensures a high degree of confidence in the structural dataset and in the derived kinematic and morphometric parameters.

4. Results

4.1. Structural dataset overview

The structural mapping of the AFS at a scale of 1:50,000 led to the identification of 3749 individual features (Fig. 3a–d). These include 395 eruptive fissures (10.5 %), 2301 extension fractures (61.4 %), 1038 normal faults (27.7 %), of which 536 dip eastward and 502 westward, and 15 caldera-bounding faults (0.4 %), the latter being excluded from subsequent analysis. The overall dataset exhibits a predominant N–S to NNE–SSW strike, with a concentration between N10°E and N20°E (Fig. 3d and 4a). The average strike is N17.5°E with a standard deviation (SD) of 15.8°. Structure lengths vary from 10 m to 13,380 m, with a mean of 445 m and SD of 792 m (Fig. 5a).

Eruptive fissures display a generally NNE–SSW orientation, with a dominant peak between N20°E and N30°E, an average strike of N27.2°E, and SD of 22.6° (Fig. 3e and 4b). Their lengths reach a maximum of 2000 m, with a mean of 314.4 m and SD of 263 m (Fig. 5b).

Extension fractures (other than eruptive fissures) show a broader N–S to NNE–SSW orientation, with a principal peak between N10°E and N20°E. The average strike is N17.2°E with SD of 14.5° (Fig. 3f and c). Lengths extend up to 4500 m, with a mean of 198 m and SD of 200 m (Fig. 5c).

Normal faults exhibit a general N–S to NNE–SSW trend, similar to the other structural subsets, with a primary peak between N10°E and N20°E (Fig. 3g and 4d). Both east- and west-dipping faults share this orientation (Fig. 3h–i, 4e–f). The full normal fault dataset has an average strike of N14.6°E (SD = 14°), with east-dipping faults averaging N14.6°E (SD = 14.3°) and west-dipping faults N14.7°E (SD = 13.5°). Normal faults are generally longer than other structures, reaching up to 13,380 m with a mean of 1042 m (SD = 1282 m) (Fig. 5d). East- and west-dipping subsets show comparable length statistics: mean values of 1041 m and 1043 m, and SDs of 1271 m and 1293 m, respectively (Fig. 5e and f).

To examine spatial patterns, strike and length data were related to UTM coordinates (Zone 28N, WGS84, hereafter displayed in kilometres instead of meters). The greatest strike variability of the whole structures occurs in the southern segments such as within the Askja caldera and along the southernmost sector of the rift, near Vatnajökull (Fig. 4a). We note that the location of this variability and complexity is found in a region of the rift zone with high obliquity to the extension direction (cf. Fig. 1). Between Y = 7,220,000 and Y = 7,260,000, structures mainly trend N–S to NE–SW. From Y = 7,260,000 to Y = 7,320,000, the dominant strike becomes N–S, with a notable NNE–SSW to NE–SW shift around Y = 7,320,000. North of Y = 7,340,000, the trend reverts to N–S, including NNW–SSE components. Two major gaps in structural data are observed at Y = 7,290,000 (associated with surface sediment cover) and Y = 7,340,000, linked to Sveinar lava flows (~11,000 yr BP) and pre-LGM units affected by glacial erosion (Sæmundsson et al., 2012).

Eruptive fissures exhibit the widest variation in strike, particularly near and south of the Askja caldera (Fig. 4b). North of the caldera, up to Y = 7,280,000, trends remain N–S to NNE–SSW. Beyond this point, eruptive features are sparse, with two isolated fissures near Y = 7,300,000 and a cluster between Y = 7,320,000 and 7,340,000, trending N–S to NNE–SSW.

Extension fractures also vary significantly in strike near the Askja caldera, though less than eruptive fissures (Fig. 4c). The spatial variability of strike near the Askja caldera may reflect localised magmatic processes. This is consistent with geodetic evidence of recent caldera deflation and inflation episodes (Parks et al., 2017), also captured in InSAR datasets from the European Ground Motion Service (Costantini

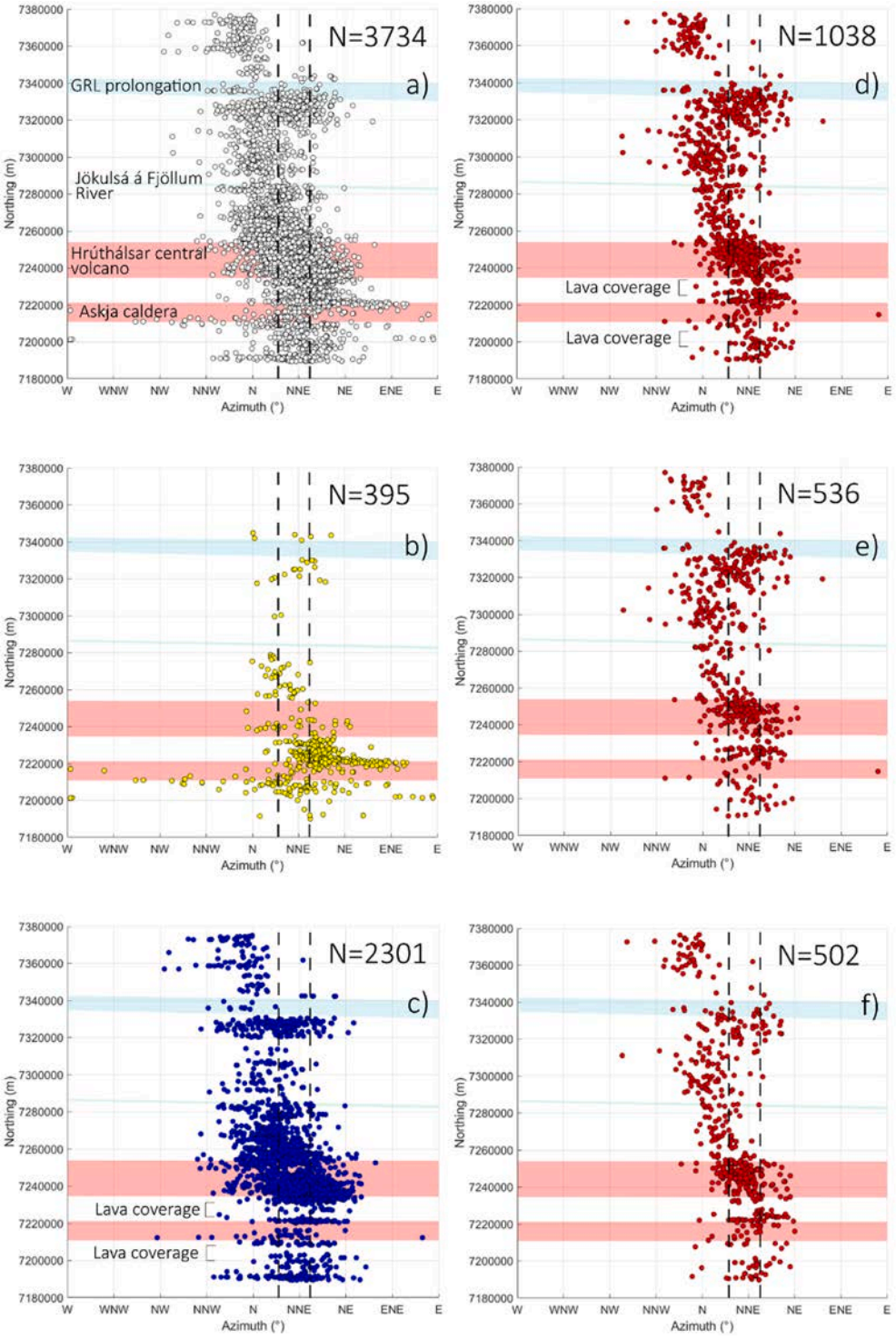

Fig. 4. Scatterplot showing the strike variation with the Y coordinates considering (a) the entire dataset, (b) eruptive fissures, (c) extension fractures, (d) normal faults, (e) E-dipping normal faults, and (f) W-dipping normal faults. Black dashed lines identify the perpendicular to the main spreading directions of the NVZ (a review of these directions is given in Corti et al., 2021). The red, green, and light blue areas identify the Askja caldera, the Jökulsá á Fjöllum River, and the prolongation of the Grímsey Lineament. (For interpretation of the references to colour in this figure legend, the reader is referred to the Web version of this article.)

et al., 2021).

North of the caldera, they shift from N–S to NE–SW, gradually rotating to N–S to NNE–SSW up to Y = 7,280,000. From Y = 7,320,000 onward, orientations include NNW–SSE and NNE–SSW. Fractures become scarce in the northernmost part of the rift, where NW–SE components appear. Dataset gaps at Y = 7,200,000 and Y = 7,230,000 correspond to lava flows aged 4500–6100 yr BP and a <4500 yr lava shield complex (Sigurgeirsson et al., 2015). Additional gaps at Y = 7, 310,000 and 7,340,000 are associated with lower fracture densities in pre-LGM units eroded by glaciers (Sæmundsson et al., 2012).

Normal faults overall trend N–S to NNE–SSW (Fig. 4d). While minor local deviations exist, variation is far less pronounced than in the dataset of eruptive fractures. Strike diversity increases within the caldera, though NNE–SSW remains dominant. Northward, faults rotate

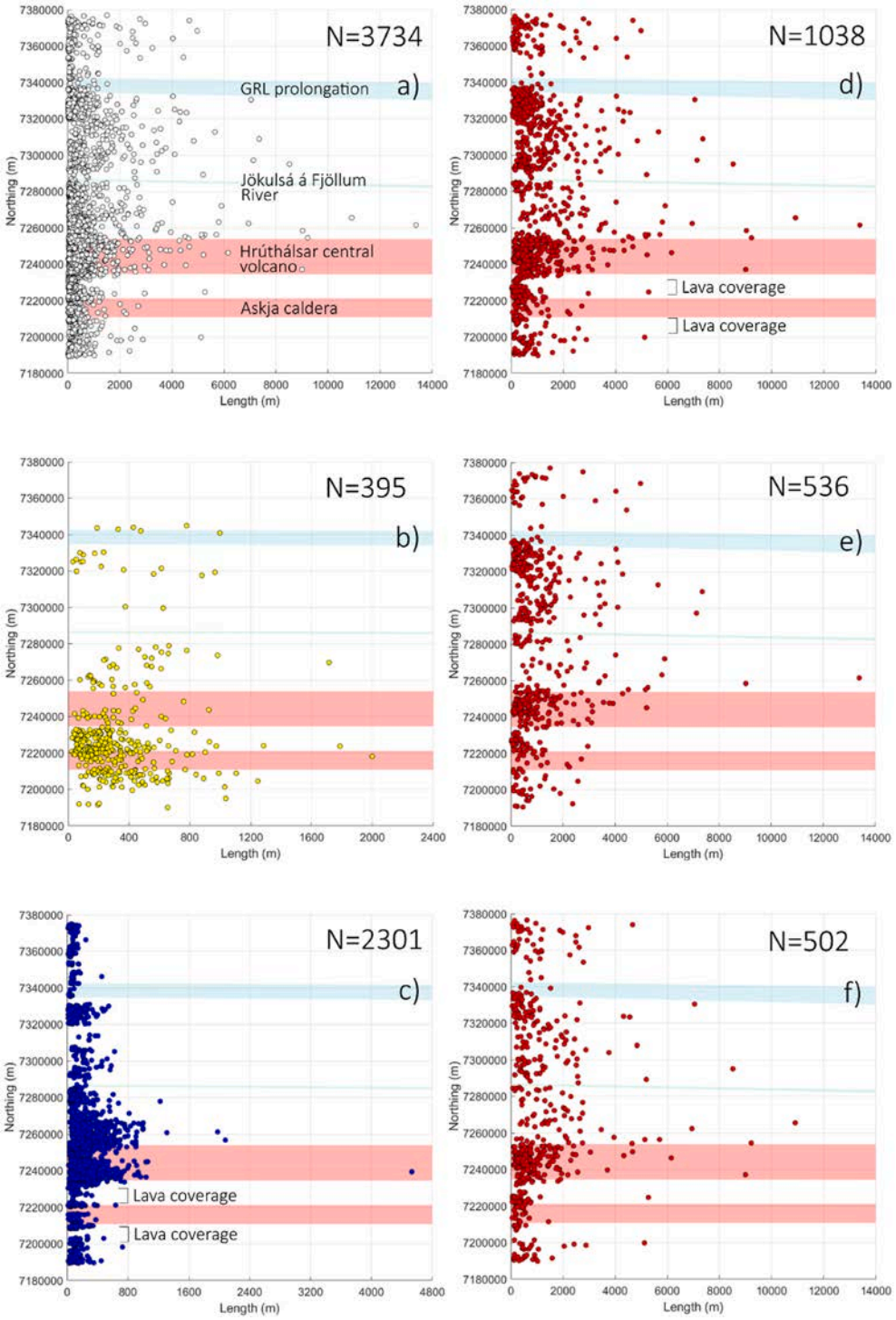

Fig. 5. Scatterplot showing the length variation with the Y coordinates considering (a) the entire dataset, (b) eruptive fissures, (c) extension fractures, (d) normal faults, (e) E-dipping normal faults, and (f) W-dipping normal faults. The red, green, and light blue areas identify the Askja caldera, the Jökulsá á Fjöllum River, and the prolongation of the Grímsey Lineament. (For interpretation of the references to colour in this figure legend, the reader is referred to the Web version of this article.)

anticlockwise to NE–SW, then back to N–S, and eventually clockwise to NNE–SSW at the northern edge. Subordinate NNW–SSE to NW–SE orientations occur around Y = 7,290,000 and 7,310,000. Gaps mirror those identified for other datasets: Y = 7,200,000, 7,230,000, and 7,340,000. East- and west-dipping faults show parallel trends (Fig. 4e and f): NNE–SSW to NE–SW up to Y = 7,260,000, transitioning to N–S until Y = 7,320,000, and then reverting to NNE–SSW to NE–SW. The northern edge displays N–S to NNW–SSE orientations. Strike variability is slightly greater within the caldera for E-dipping faults, and both subsets show NNW–SSE orientations near Y = 7,310,000.

Length distributions across the fissure swarm are heterogeneous (Fig. 5a). The highest values are concentrated between Y = 7,240,000 and Y = 7,280,000, coinciding with a <7000 yr-old lava shield complex and hyaloclastite unit. Elevated lengths are also noted around Y = 7,300,000, Y = 7,320,000, and in the northernmost rift sector. Eruptive fissures are concentrated in the central–southern part of the rift.

Maximum lengths occur within the Askja caldera, reaching 2000 m (Fig. 5b), while fissures elsewhere typically remain below 800 m. Extension fractures show maximum lengths between Y = 7,230,000 and Y = 7,270,000 (Fig. 5c), with minor increases near Y = 7,300,000 and 7,320,000.

Normal faults are longer in the central rift, peaking near Y = 7,260,000 (Fig. 5d), with a secondary maximum around Y = 7,300,000, and elevated lengths also observed in the northernmost zone. East- and west-dipping faults mirror this distribution (Fig. 5e and f), with the longest segments located centrally (Y = 7,260,000) and local peaks in the northern rift.

The spatial distribution of structural orientations within the ASF was also evaluated as a function of X coordinate (UTM 28N). Overall, the swarm displays a dominant N–S to NNE–SSW orientation (Fig. 6a). In the westernmost sector, the trend transitions from N–S/NNE–SSW to NNE–SSW/NE–SW up to X = 420,000. Eastward of this point,

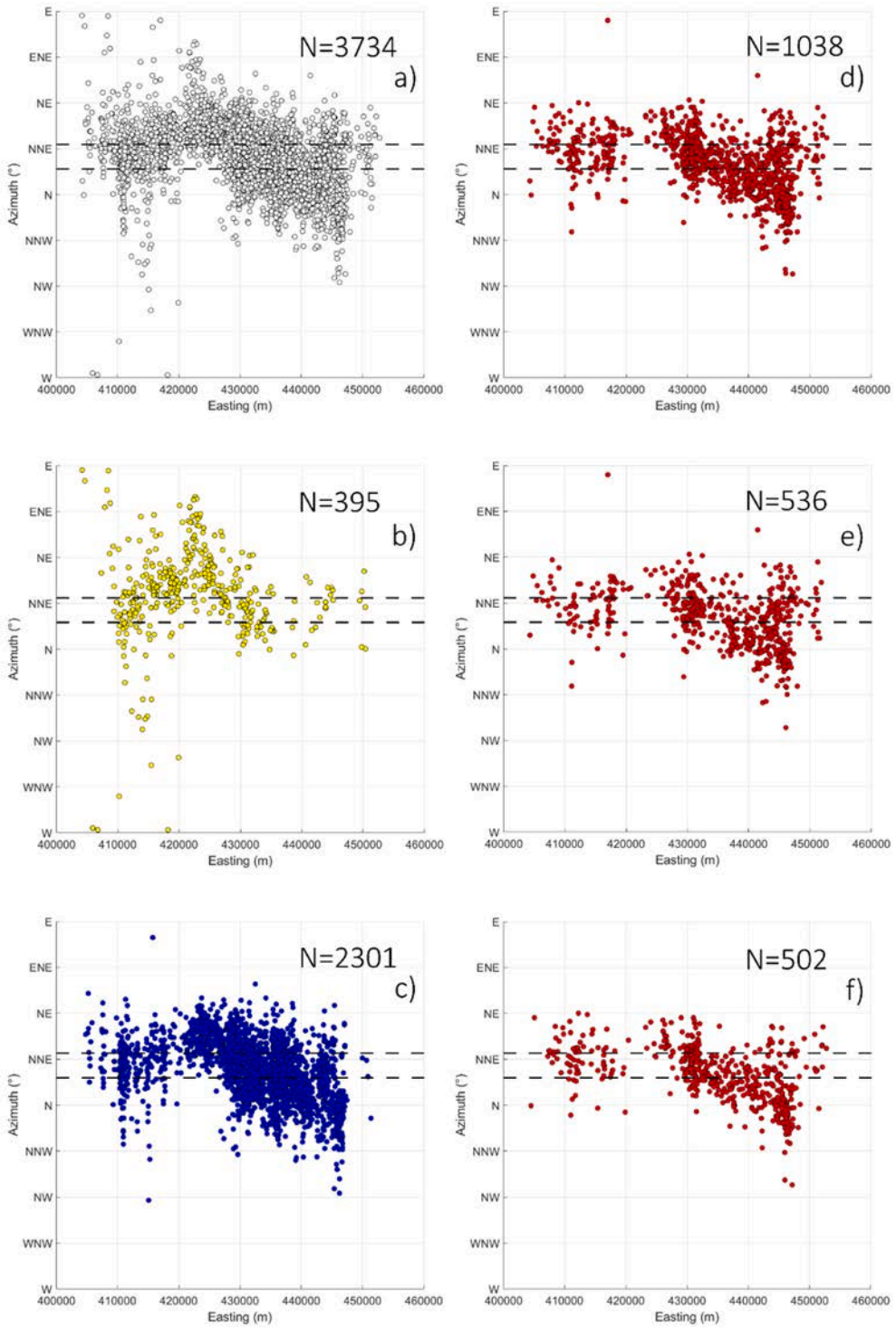

Fig. 6. *Scatterplot showing the azimuth variation with the X coordinates considering (a) the entire dataset, (b) eruptive fissures, (c) extension fractures, (d) normal faults, (e) E-dipping normal faults, and (f) W-dipping normal faults. Black dashed lines identify the perpendicular to the main spreading directions of the NVZ (a review of these directions is given in* Corti et al., 2021*).*

orientations progressively rotate to a N–S to NNW–SSE trend toward the eastern margin of the rift. Eruptive fissures exhibit notable variability in orientation, particularly in the western portion, where the Askja caldera is located (Fig. 6b). Between X = 420,000 and 425,000, orientations are mostly NNE–SSW, with a subordinate ENE–WSW component. East of X = 430,000, the dominant trend becomes consistently NNE–SSW. These structures are most abundant in the central and western sectors and become less frequent toward the east. Extension fractures are more developed in the eastern part of the rift, and less frequent in the west (Fig. 6c). In the western sector, orientations predominantly range from N–S to NE–SW, with local NNW–SSE components. Moving eastward from X = 420,000, a gradual anticlockwise rotation is observed, shifting from NE–SW/NNE–SSW to a dominant N–S/NNW–SSE trend. Normal faults are similarly concentrated within the eastern half of the rift (Fig. 6d). In the western sector, orientations are mainly NNE–SSW, with subordinate NE–SW trends. Approaching X = 430,000, faults display N–S to NE–SW strikes, evolving toward N–S/NNE–SSW by X = 440,000. A broader range of orientations is recorded near X = 445,000, where

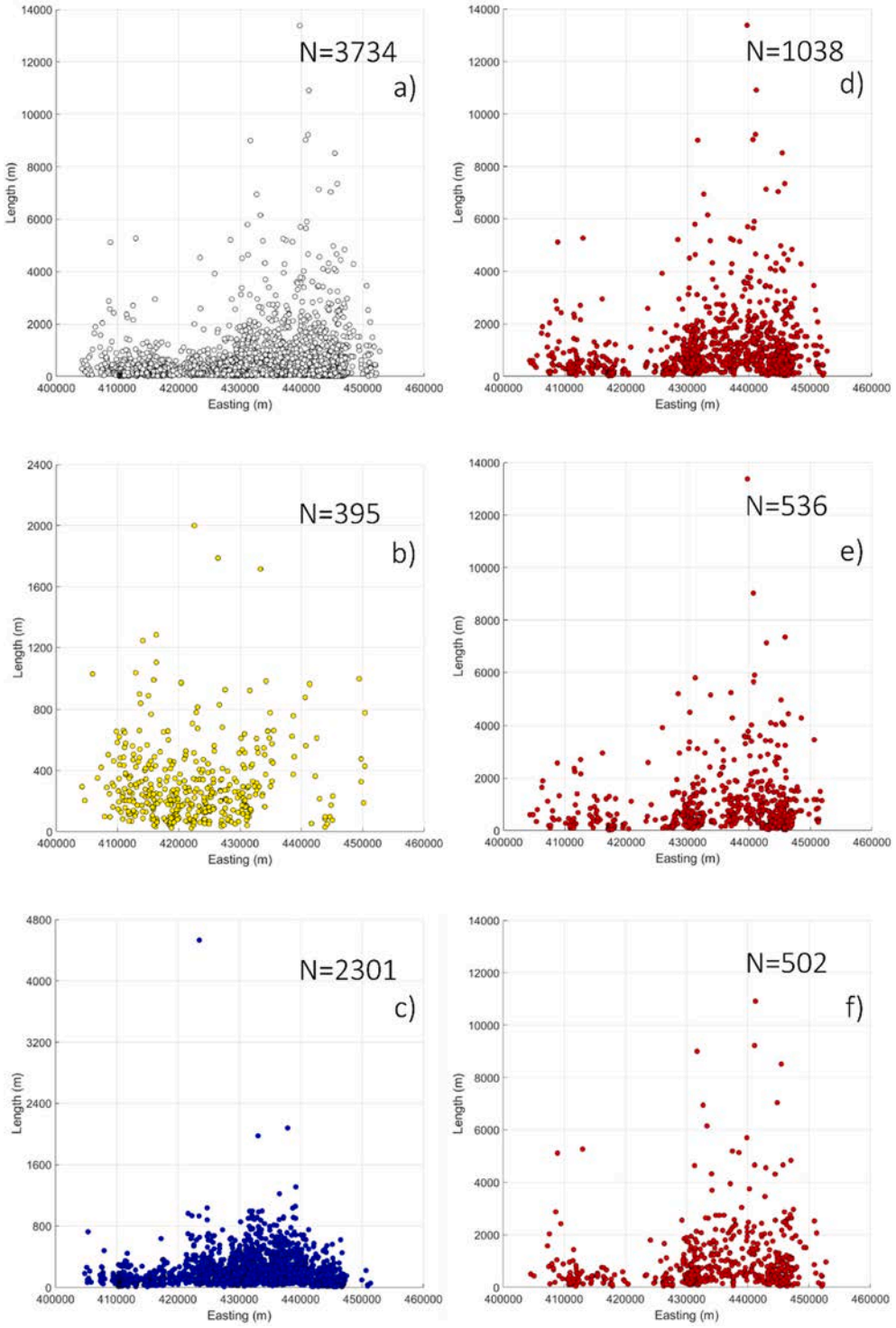

Fig. 7. Scatterplot showing the length variation with the X coordinates considering (a) the entire dataset, (b) eruptive fissures, (c) extension fractures, (d) normal faults, (e) E-dipping normal faults, and (f) W-dipping normal faults.

structures trend N–S to NNE–SSW, with NE–SW and NNW–SSE components.

Both east- and west-dipping normal faults show similar spatial patterns (Fig. 6e and f). In the west, orientations are dominantly NNE–SSW. From X = 430,000 to the rift's eastern limit, strikes transition from NNE–SSW/NE–SW to N–S/NNE–SSW, with localized increases in orientation variability near X = 445,000, where NE–SW and NNW–SSE trends are also observed.

Structure lengths are spatially variable across the rift (Fig. 7a). A general increase in length values is observed moving eastward, with maxima near X = 430,000 and X = 440,000.

Eruptive fissure lengths vary across the rift (Fig. 7b). Most features are <400 m in length. However, near X = 415,000 in the western portion, a local increase is observed. Despite their reduced frequency in

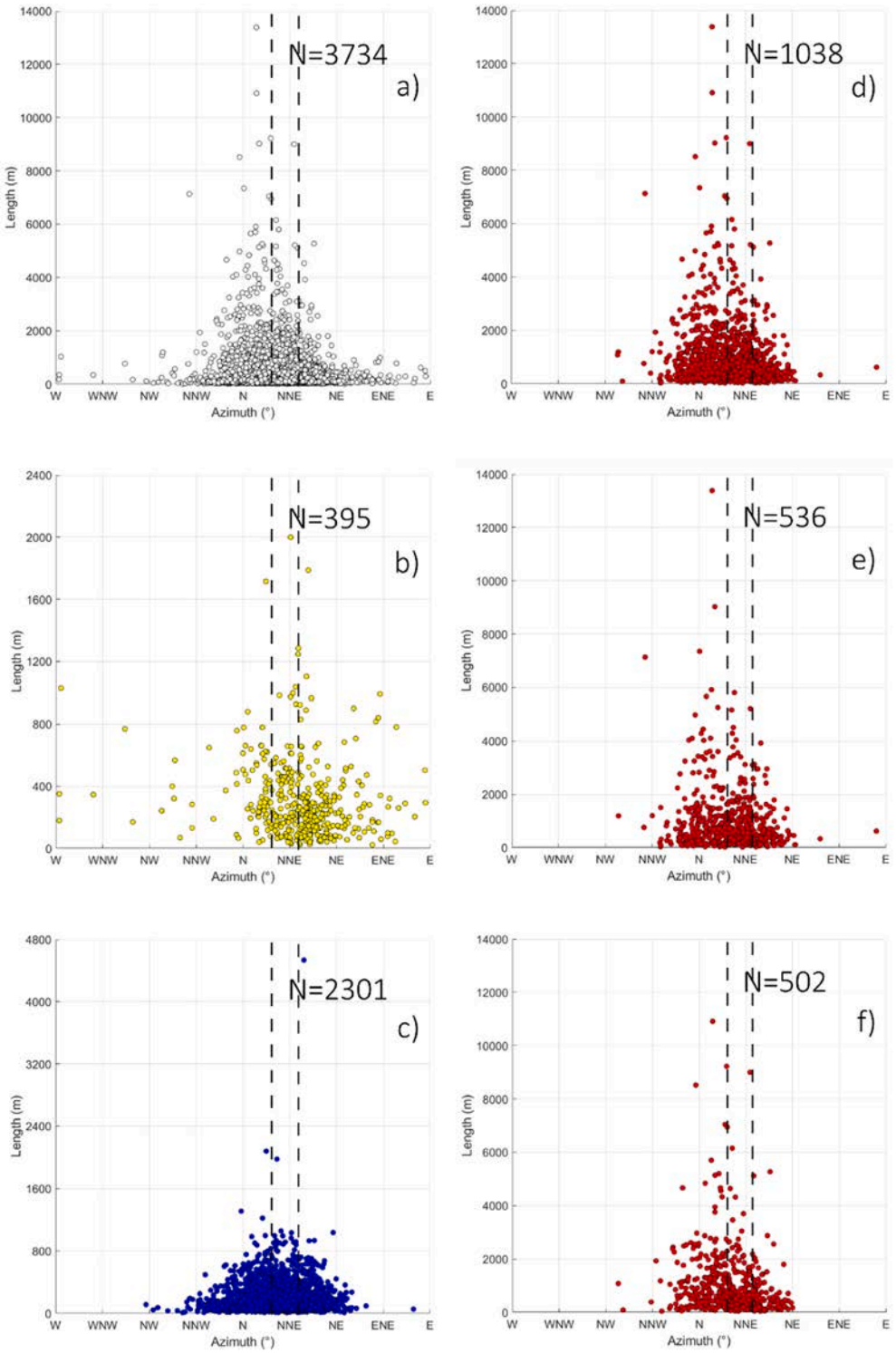

Fig. 8. Scatterplot showing the relation between azimuth and length values considering (a) the entire dataset, (b) eruptive fissures, (c) extension fractures, (d) normal faults, (e) E-dipping normal faults, and (f) W-dipping normal faults. Black dashed lines identify the perpendicular to the main spreading directions of the NVZ (a review of these directions is given in Corti et al. (2021).

the eastern rift, eruptive fissures in this area tend to be longer. Extension fractures reach their maximum lengths in the eastern sector of the rift (Fig. 7c). Lengths increase from the western boundary up to X = 430,000–440,000, followed by a gradual decrease toward the easternmost edge.

Normal faults also display their longest lengths in the eastern portion (Fig. 7d). From the rift's western limit to X = 420,000, lengths decrease, followed by a zone of sparse faulting until X = 430,000. Beyond this point, lengths increase up to X = 440,000, where the longest faults are recorded. Both east- and west-dipping faults show comparable trends (Fig. 7e and f). Lengths decline eastward up to X = 420,000, then increase again between X = 430,000 and 440,000, before slightly decreasing toward the rift's eastern margin.

The relationship between structure orientation and length was also assessed. Overall, the longest structures in the dataset are aligned N–S to NNE–SSW (Fig. 8a). For eruptive fissures, no clear correlation emerges due to significant azimuthal variability (Fig. 7b), although the longest examples also strike NNE–SSW. Extension fractures, in contrast, show a consistent pattern: the longest fractures are associated with NNE–SSW orientations (Fig. 8c). The normal fault dataset, including both east- and west-dipping subsets, exhibits a clear correlation between length and orientation: longer faults tend to strike N–S to NNE–SSW (Fig. 8d–f), and become shorter both clockwise and counterclockwise.

4.2. Fracture intensity, rift width and dilation

Fracture intensity within the AFS was assessed using a set of 382 parallel transects, each arbitrarily spaced 500 m apart and oriented along a N106°E azimuth, i.e. sub-parallel to the main regional extension direction (Fig. 9). Here, fracture intensity corresponds to the cumulative number of intersecting structures recorded along each transect. The length of each transect corresponds to the distance between the two outermost structures intersecting each N106°E-striking transects, i.e. the rift width. The analysis was first conducted on the entire structural dataset (Fig. 10a), and subsequently broken down by structural type: eruptive fissures (Fig. 11a), extension fractures (Fig. 12a), and normal faults, including the classification by dip direction (Fig. 12a and 13d–e). In addition to intensity, the rift width was measured along each transect by calculating the distance between the westernmost and easternmost intersected structures (Fig. 10b). A second set of width measurements was also computed considering only structures of the same type (e.g., fissures only), referred to as "width" in the corresponding graphs. Dilation was also estimated along each transect by extrapolating total fault heave, assuming a mean dip angle of 75°, consistent with the geometry of Pleistocene to Holocene normal faults in Iceland (Forslund and Gudmundsson, 1991) (Fig. 13c).

The maximum observed fracture intensity for the complete dataset was 39 structures, recorded along transect 249 (Fig. 10a). Fracture distribution across the rift is notably heterogeneous. Starting from the northern edge, intensity gradually increases up to transect 13 (7 structures), followed by a decrease until transect 52. From transect 56 to 249, a general increasing trend is observed, although local deviations from this pattern are present. A marked reduction in structural count occurs between transects 171 and 182, likely due to surface cover masking structural expression. After the peak at transect 249, intensity slightly declines, despite this zone having the overall higher concentration of structures. Another intensity increase occurs after transect 298, approaching the Askja caldera, where a sharp drop in fracture count is again observed. South of the caldera, structure intensity initially falls (up to transect 350), followed by a moderate increase toward the southernmost end of the rift (up to 10 structures per transect).

Rift width shows a similar non-uniform pattern. The widest sections are located in the central rift sector and in proximity to the northern boundary of the Askja caldera (Fig. 10b). From the northern margin up to transect 277, width progressively increases, peaking locally at 15.4 km. Between transects 277 and 295, width decreases. It then increases

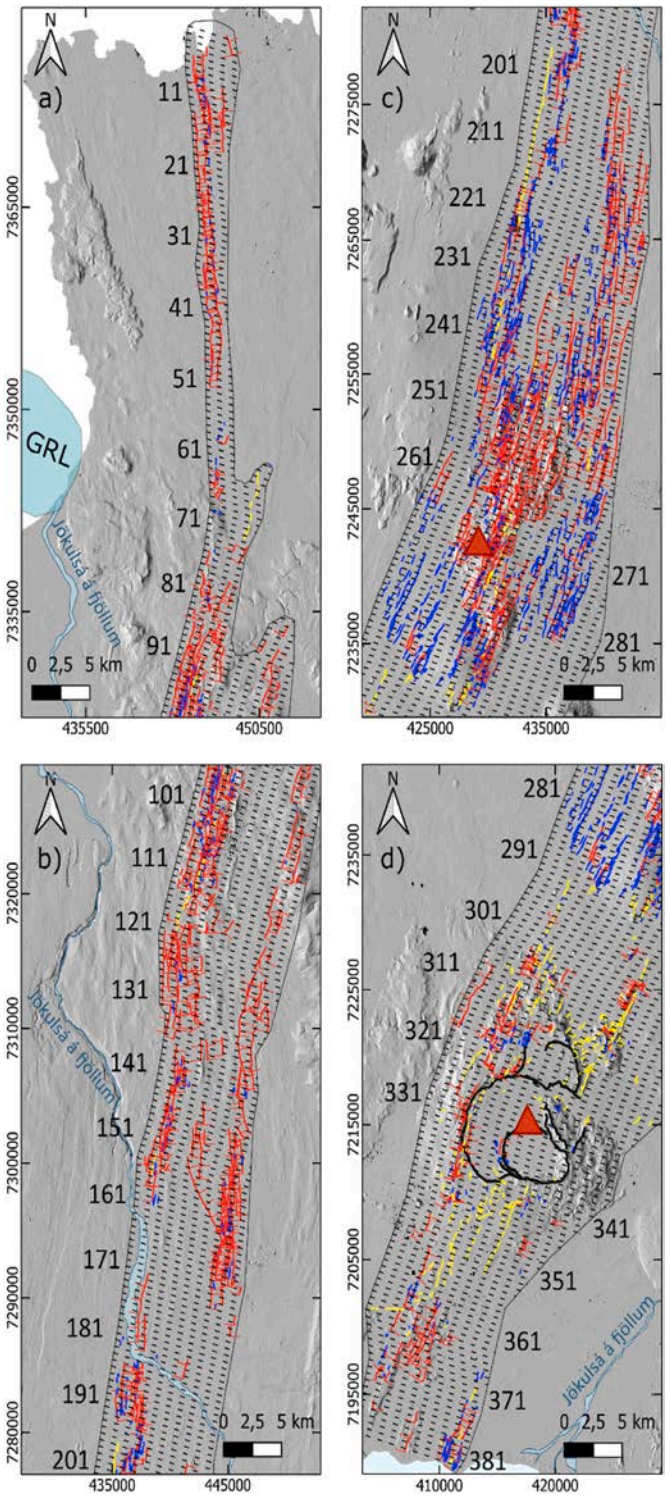

Fig. 9. Map showing the AFS dataset and the 382 N106°E transects (black dashed lines), defined for the evaluation of the total number of structures, and the rift width. The light blue area on the southern edge of the rift indicates the Vatnajökull Glacier. Original photogrammetry-derived DSMs and the ArcticDEM v.4.1 (Porter at el., 2023) are used as a background. The area is the same as Fig. 2 and is located in Fig. 1. (For interpretation of the references to colour in this figure legend, the reader is referred to the Web version of this article.)

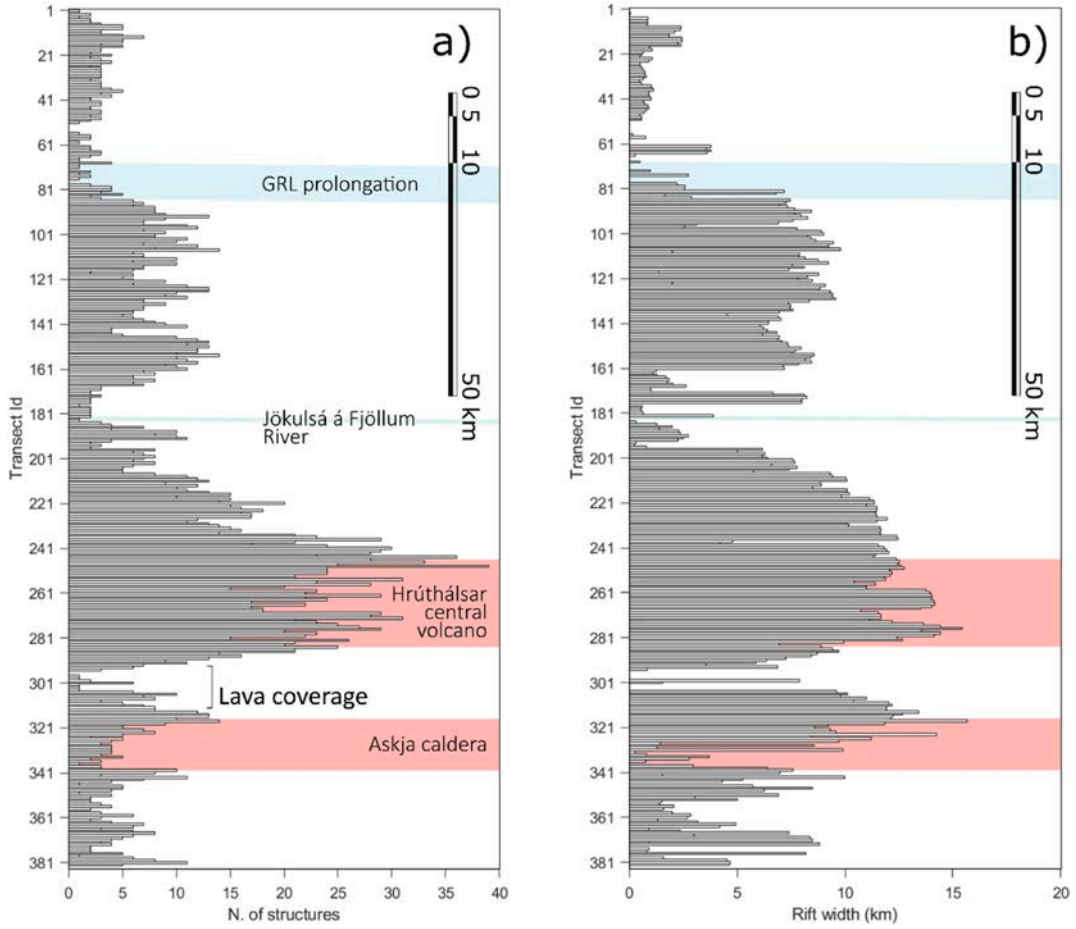

Fig. 10. Graphs showing (a) the total number of structures and (b) the rift width. The light red areas define the Askja Caldera and the Hrúthálsar Central Volcano, whereas the light blue and the green ones represent the prolongation of the Grímsey Lineament and the Jökulsá á Fjöllum River, respectively. (For interpretation of the references to colour in this figure legend, the reader is referred to the Web version of this article.)

again from transect 301 toward the caldera's northern edge, where the maximum width of 15.6 km is recorded at transect 318. Within the Askja caldera, rift width narrows significantly, followed by a minor broadening near its southern rim, although this might be considered a result of coverage and structure obscuration by young volcanic materials. Southward from this point, the rift narrows again until transect 361, beyond which a slight increase is observed in the southernmost sector.

Eruptive fissures are predominantly located in the southern sector of the Askja Rift (Fig. 11a). In the northern portion, isolated fissures are observed, particularly along transects 62, 120, and 154–156, where they are spatially associated with the Sveinar lava flows (~11 ka) (Sæmundsson et al., 2012). From transect 197 onward, the number of eruptive fissures increases, culminating at transect 315 (northern edge of the Askja caldera) with a peak of seven fissures. Between transects 197 and 283, the average number of eruptive fissures per transect is around 1, occasionally reaching 3, particularly in zones corresponding to the <7000-yr-old lava shield complex and the base of hyaloclastite ridges (Sæmundsson et al., 2012). Within the Askja central volcano (transects 301–365), fissure frequency remains high, although it decreases significantly within the caldera. From the southern caldera edge to transect 359, a decline in fissure occurrence is observed. In the southernmost part of the rift (transects 370–382), few eruptive fissures are present; all are related to the 2014–2015 Bárðarbunga dyke intrusion (Sigurgeirsson et al., 2015).

The maximum distance between the outermost eruptive fissures within each transect was also evaluated (Fig. 11b). The greatest distances, up to ~11 km, occur within the Askja central volcano, specifically at transects 308 and 326, predominantly on the northern flank. At the southern edge of the edifice, fissure width decreases. In the northern rift, fissures are fewer and aligned within grabens, resulting in null width values up to transect 241.

Extension fractures are primarily distributed in the central sector of the rift (Fig. 12a). The northern portion (up to transect 170) is characterised by a low frequency of these features. From transect 170, their number gradually increases, reaching a peak of 20 fractures at transect 245. A decrease follows until transect 257, after which fracture counts increase again, peaking at 19 fractures at transect 285. These fractures are concentrated in the <7000-yr-old lava shield complex, the area also showing maximum fracture intensity. Conversely, fracture occurrence diminishes in the hyaloclastite-dominated terrain between transects 245 and 257. South of the lava shield zone, fracture intensity reduces, and in the southern rift, only a limited number of extension fractures are present.

The width of the extension fractures swarm (Fig. 12b) is greatest in the central rift sector, reaching up to 15.4 km at transect 277. Width values are near zero in the northern rift, except for minor increases between transects 141 and 161. After transect 185, width gradually increases, peaking at transect 277, and then diminishes toward transect 293. The southern sector maintains generally low width values.

Normal faults are present throughout the entire AFS (Fig. 13a). Fault intensity increases from the northern margin, reaching a local peak of 7 faults at transect 13, followed by a decline until transect 51. Between transects 51 and 79, fault counts are minimal. Thereafter, fault frequency increases irregularly, peaking at 26 faults at transect 257. A progressive decline is observed toward transect 292, beyond which fault frequency remains low. This reduction may be linked to lava flows from

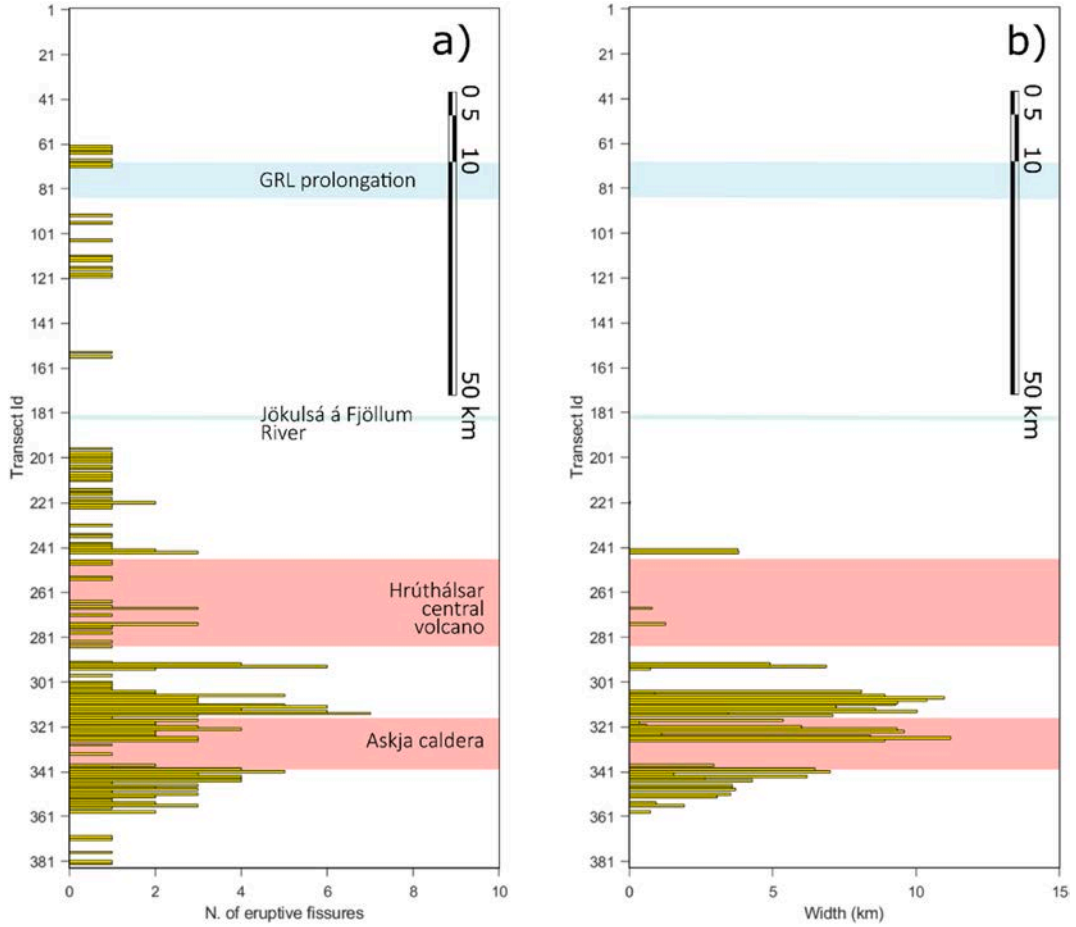

Fig. 11. Graphs showing (a) the total number of eruptive fissures and (b) the width of the fissure swarm. The light red areas define the Askja Caldera and the Hrúthálsar Central Volcano; the light blue and the green ones represent the Grímsey Lineament prolongation and the Jökulsá á Fjöllum River, respectively. (For interpretation of the references to colour in this figure legend, the reader is referred to the Web version of this article.)

the central volcano obscuring underlying fault structures. The highest fault intensity occurs in the hyaloclastite hills (transects 246–286), with intensity decreasing away from this core zone.

The pattern of east-dipping normal faults (Fig. 13d) generally mirrors that of the total fault population. intensity increases from the northern edge toward the hyaloclastite mountains, followed by a decline up to transect 291. A minor local peak (5 faults) appears at transect 306, then fault frequency decreases further toward the southern limit.

West-dipping normal faults (Fig. 13e) similarly show a steady increase from the north to the hyaloclastite region, with local gaps between transects 50–80 and 170–181. In the southern rift, their distribution is lower and irregular.

The distance between the outermost normal faults per transect (Fig. 13b) varies significantly. Smaller widths of the fault swarm are observed in the northern sector, decreasing to zero at transect 64. Width then increases, averaging ~7 km between transects 79 and 160. A reduction occurs between transects 161 and 181, likely due to surface cover, after which width gradually increases, reaching a maximum of 14 km at transect 262 (coinciding with the hyaloclastite zone) before decreasing outward. Width remains elevated north of the Askja caldera and decreases southward, with a pronounced drop within the caldera itself.

Dilation estimates based on the calculated heave from normal faults (Fig. 13c) indicate maximum values in the central rift, particularly within the hyaloclastite hills and lava shield complex, and declining outward from this zone. In the northern sector (transects 1–61), dilation averages 0.7 m. From there, dilation rises to transect 147, interrupted between transects 130–145, followed by a decrease until transect 169. Between transects 170 and 231, values remain low. Dilation increases again from transect 237, peaking at 49 m at transect 255, before declining to zero after transect 292. A further increase is observed between transects 299 and the Askja caldera, followed by a decrease southward.

Finally, maximum throw values derived from the full normal fault dataset (Fig. 14) are lowest in the northern sector (1–7 m), increase southward, and reach >10 m in the hyaloclastite hills north of Askja. Isolated high throws are also recorded within the central volcano, while the southernmost rift is characterised by low throw values. Notably, the largest throws correspond to areas of elevated topography.

4.3. Along-axis deformation and slip profiles

To assess the overall along-axis deformation within the AFS, we analysed a total of 150 normal faults (Fig. 15). The results reveal that the majority of the measured slip profiles (n = 64; 42.6 %) exhibit a northward tapering geometry. In contrast, 44 profiles (29.3 %) taper southward, 18 profiles (12 %) are symmetrical, and 24 profiles (16 %) could not be confidently classified. As example, we report in Fig. 16 two asymmetric slip profiles with respect to one symmetric profile. The two asymmetric profiles show clear tapering northward or southward.

When considering the cumulative lengths of the faults in each category, northward-tapering profiles account for 224.6 km, whereas southward-tapering profiles represent 145.7 km. These results demonstrate a predominance of northward-tapering profiles, both in terms of total number and cumulative fault length.

Within the AFS, the main Askja central volcano is positioned near its

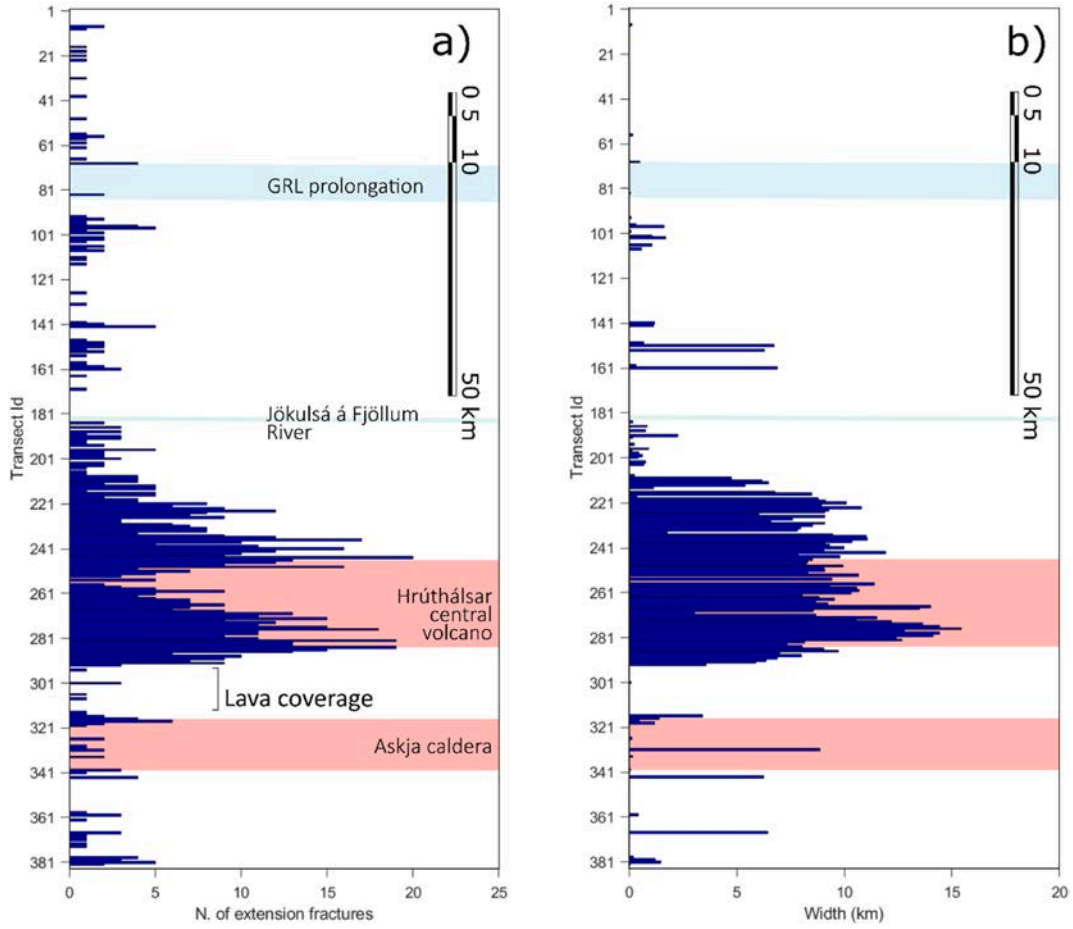

Fig. 12. Graphs showing (a) the total number of extension fractures, (b) the width of the extension fracture swarm. The light red areas define the Askja Caldera and the Hrúthálsar Central Volcano, whereas the light blue and the green ones represent the prolongation of the Grímsey Lineament and the Jökulsá á Fjöllum River, respectively. (For interpretation of the references to colour in this figure legend, the reader is referred to the Web version of this article.)

southernmost margin. Additionally, the northern extent of the Vatnajökull Glacier lies approximately 21 km southwest of the Askja volcano, thereby limiting the possibility of conducting structural analysis further to the south. This context implies a scarcity of analysable faults situated south of Askja, precluding the development of a comparable symmetrical analysis south of this volcano with respect to north of it.

5. Discussion

In the following sections, we discuss the implications of the quantitative results presented in Section 4, focusing on how the observed spatial patterns in structure orientation, length, fracture intensity, dilation, and fault slip profiles constrain rift propagation and magma-driven deformation within the AFS.

5.1. Rift fracture distribution as expression of central volcano

In volcanotectonic settings, surface fracture swarms are typically the result of extensional tectonics associated with rifting episodes and dyke intrusions. These features develop in response to regional tensile stress fields acting on the brittle upper crust, leading to the formation of aligned fractures and the emplacement of magma along zones of weakness. Numerous studies have shown that such fracture systems often represent the surface expression of deeper magmatic processes and reflect the structural configuration of the underlying plumbing system (Walker, 1965; Gudmundsson, 1983; Tibaldi et al., 2013; Tibaldi, 2015). The concept of dyke-induced faulting within volcanic rifts has been well established by numerous studies (Pollard et al., 1983; Rubin and Pollard, 1988; Rubin, 1992; Trippanera et al., 2015; Acocella and Trippanera, 2016; Xu et al., 2016), and has been directly confirmed by observations during recent rifting episodes at the Krafla (1975–1984) and Bárðarbunga (2014–2015) systems in Iceland. These events were marked by the formation and reactivation of normal faults and tensile fractures (Björnsson et al., 1979; Sigurdsson, 1980; Björnsson, 1985; Rubin, 1992; Hollingsworth et al., 2013; Hjartardóttir et al., 2016a; Ruch et al., 2016).

Within the AFS, the dataset of 3749 mapped structures reveals a systematic decrease in fracture intensity, rift width, and fault displacement away from the Hrúthálsar central volcano (Section 4.2; Figs. 10–13).

This zone exhibits the highest intensity of normal faults, as well as peak values of fault vertical displacement and horizontal dilation, which progressively decrease in both the northern and southern directions. Extension fractures are predominantly found within lava shields older than 7000 yrs in the vicinity of Hrúthálsar, and diminish away from this zone. Based on our data, we remark that eruptive fissures are concentrated near the Askja caldera but are also frequent in the Hrúthálsar region. These observations support the existence of a magmatic source also beneath Hrúthálsar, from which dykes propagate into the surrounding rift. As highlighted in the literature, as dykes propagate vertically and also (or mainly) laterally along rift zones, their depth is expected to increase with distance from the source, reducing the likelihood of surface eruptions (Hollingsworth et al., 2012). This mechanism aligns with the observed decline in eruptive fissures away from both the Askja and Hrúthálsar centers. Furthermore, dyke tip depth influences both the magnitude and spatial pattern of surface deformation

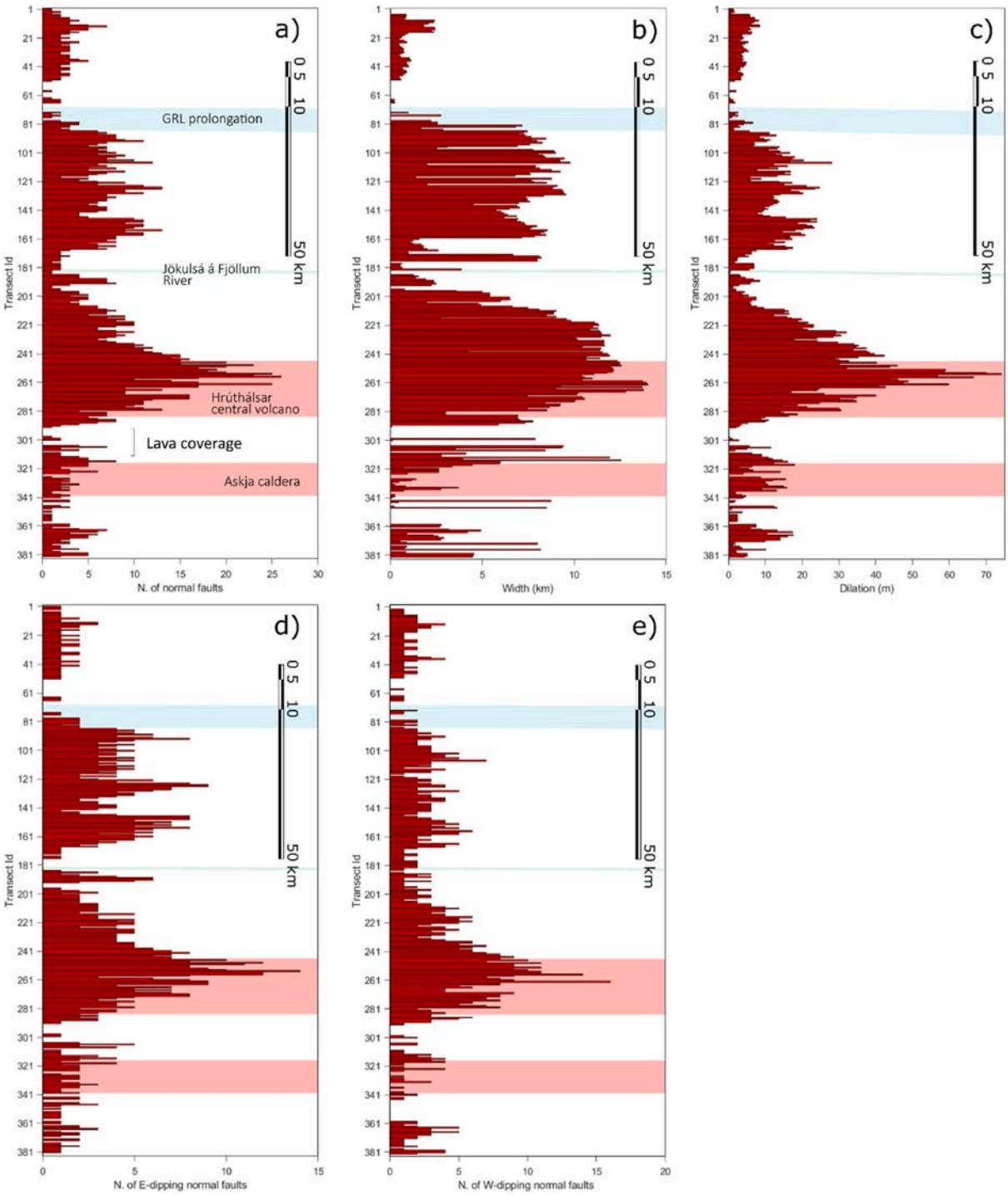

Fig. 13. Graphs showing (a) the total number of normal faults, (b) the width of the fault swarm, and (c) the dilation along each transect. The total numbers of (d) E-dipping and (e) W-dipping normal faults are also displayed. The light red areas define the Askja Caldera and the Hrúthálsar Central Volcano, whereas the light blue and the green ones represent the prolongation of the Grímsey Lineament and the Jökulsá á Fjöllum River, respectively. (For interpretation of the references to colour in this figure legend, the reader is referred to the Web version of this article.)

(Trippanera et al., 2015; Acocella and Trippanera, 2016). Consequently, reductions in fracture intensity and rift width are coherent with increasing distance from the magmatic source.

Dyke injection can also generate localised compressional stresses, potentially inhibiting further propagation and promoting dyke clustering near the source (Gudmundsson, 2003, 2020; Buck et al., 2006; Andrew and Gudmundsson, 2008; Ruz et al., 2020; Corti et al., 2023). Hjartardóttir and Einarsson (2015) documented fracture patterns across multiple lava shields within the Northern Volcanic Zone, noting that deformation within the Kollóttadyngja lava shield (south of Hrúthálsar) was more consistent with intrusions sourced from Hrúthálsar than from Askja. Additionally, considering our dataset, no significant changes in fracture azimuths were observed near Hrúthálsar, indicating that the regional stress regime remains dominant. This is consistent with expectations for edifices less than ~3 km in height, which are unlikely to produce radial stress fields (Acocella and Neri, 2009).

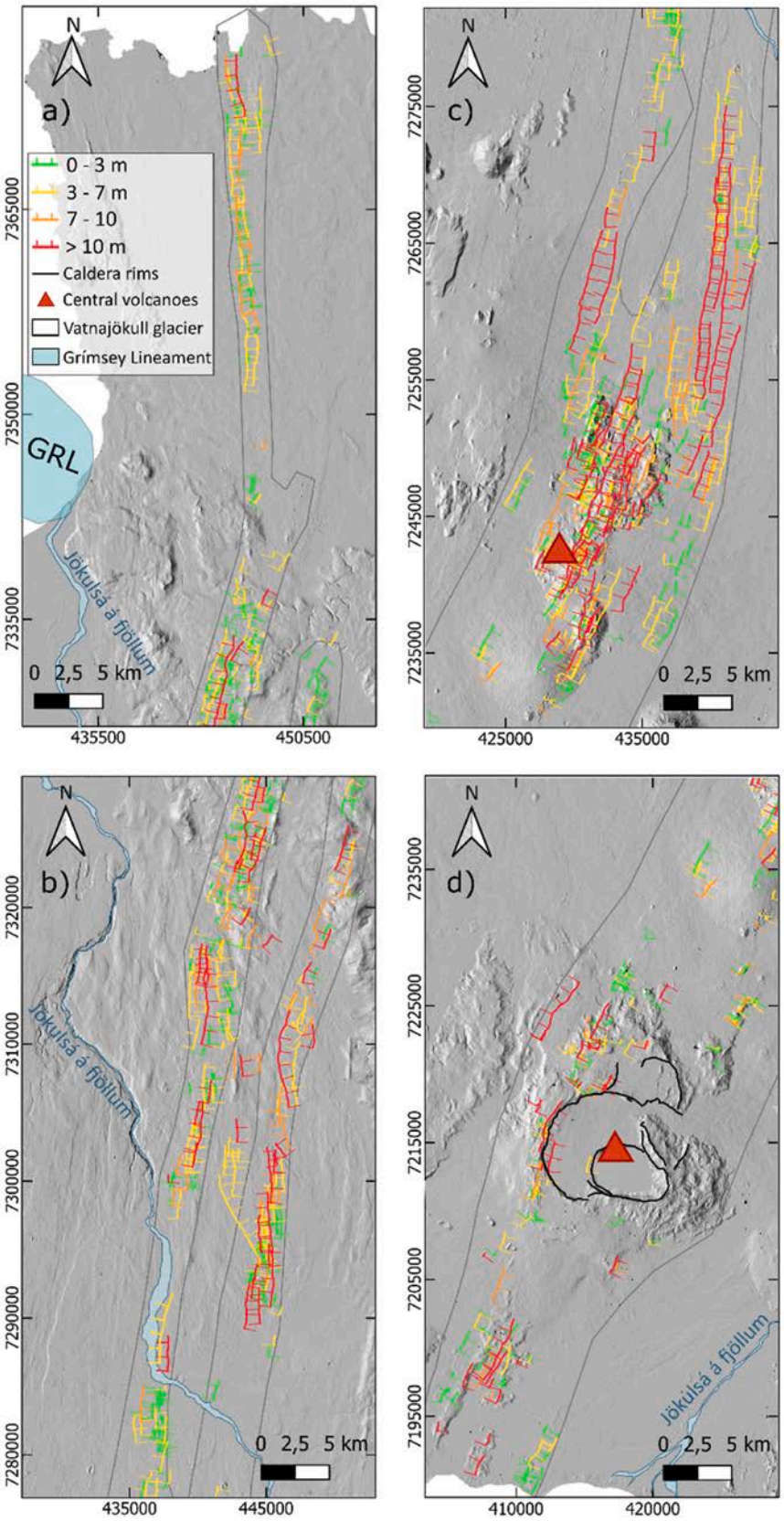

Fig. 14. Map showing normal faults classified within different ranges of maximum throws. Ticks are on the downthrown side of the scarps. The white area on the southern edge of the rift indicates the Vatnajökull Glacier. Original photogrammetry-derived DSMs and the ArcticDEM v.4.1 (Porter at el., 2023) are used as a background. The area is the same as previous maps and is located in Fig. 1.

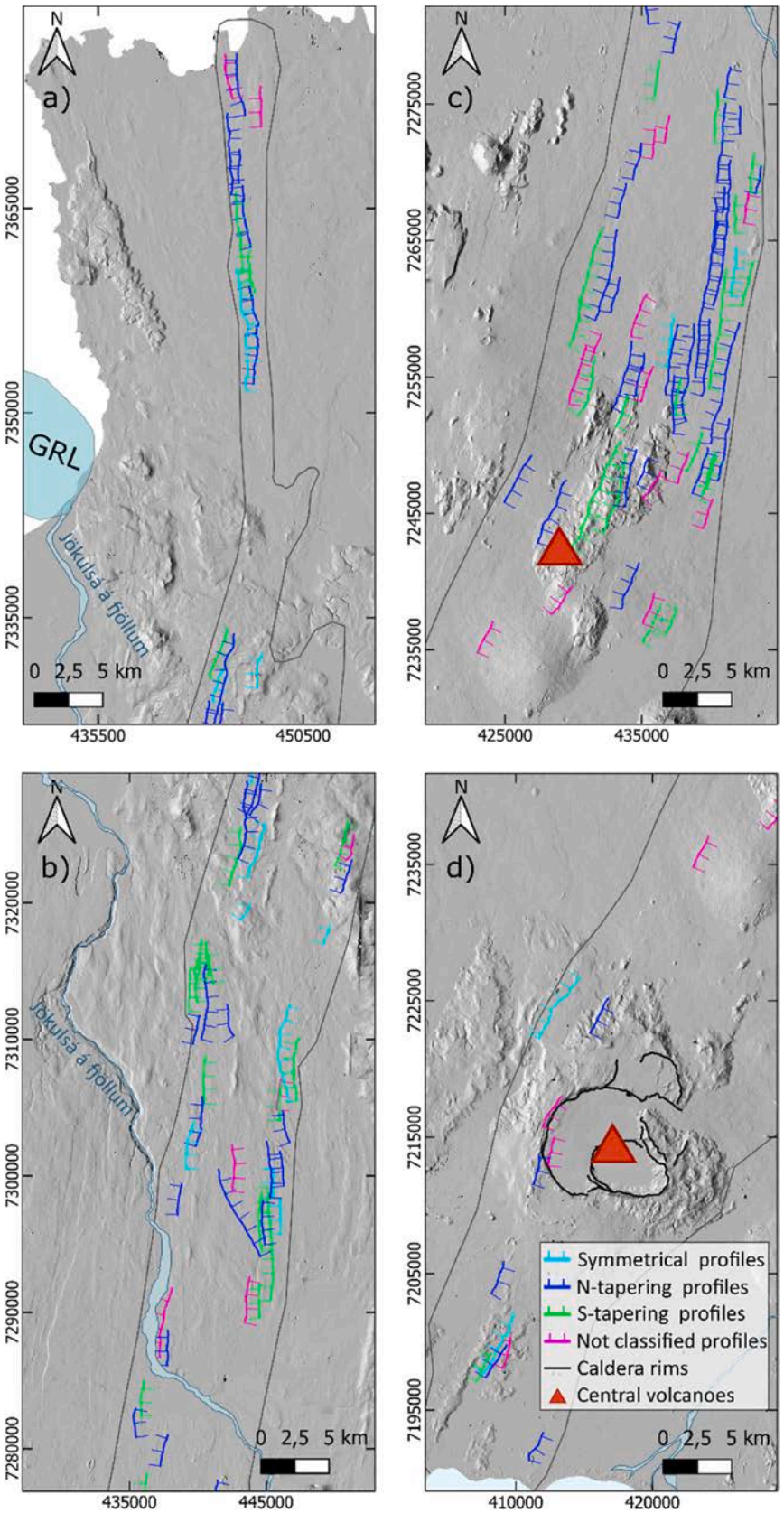

Fig. 15. Map illustrating the fault-slip profile analysis conducted within the AFS. Ticks indicate the downthrown side of each normal fault. The light blue-shaded area at the southern boundary of the rift corresponds to the Vatnajökull Glacier. The background imagery consists of original photogrammetry-derived Digital Surface Models (DSMs) and ArcticDEM version 4.1 (Porter et al., 2023). The area is the same as previous maps and is located in Fig. 1. (For interpretation of the references to colour in this figure legend, the reader is referred to the Web version of this article.)

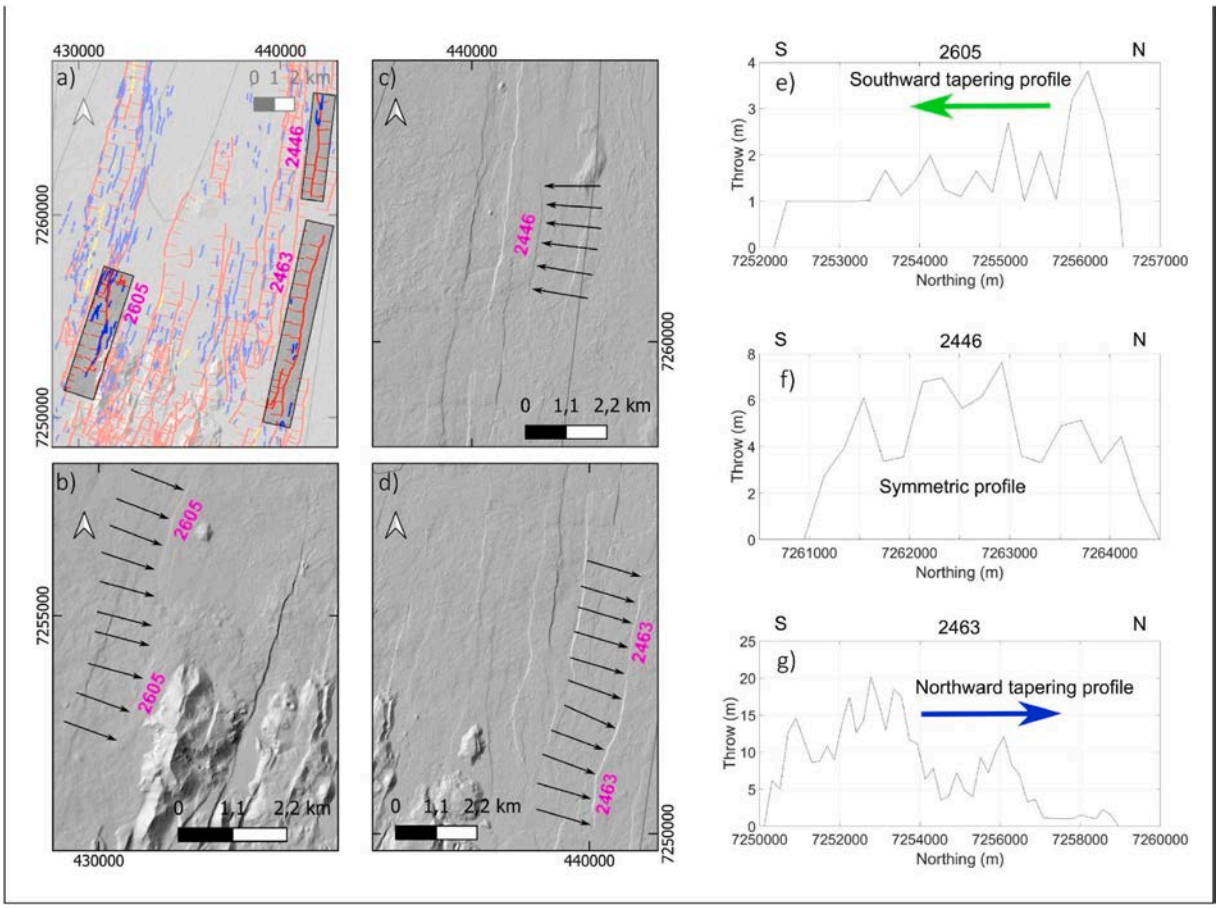

Fig. 16. Examples of fault slip profiles along the Askja Fissure Swarm. (a) Location map of the analysed faults; the highlighted areas correspond to the faults shown in b–d. (b–d) Hillshade views of three representative normal faults, showing fault traces where the fault scarp is highlighted by black arrows; fault IDs are indicated in magenta. (e–g) Slip (throw) profiles extracted from the faults in b–d, respectively, illustrating (e) southward-tapering, (f) symmetric, and (g) northward-tapering profiles. Panels e–g are all located within the area shown in a.

Our observations on new data are also consistent with the data collected during the Krafla rifting episode, which has been interpreted as a consequence of laterally propagating dykes sourced from a shallow magma chamber, with earthquake swarms radiating from the caldera to the surrounding fissure swarms (Brandsdóttir and Einarsson, 1979; Einarsson and Brandsdóttir, 1980). Similarly, along the outer margins of the Askja caldera there are several aligned vents and dikes that strike NNE, parallel to the AFS (Trippanera et al., 2018). Stress concentrations are expected to develop in proximity to magma chambers, thereby promoting dyke nucleation (Gudmundsson, 1988). Accordingly, the frequency of dyke intrusions typically diminishes with increasing distance from the magmatic source (Walker, 1958, 1960; Helgason and Zentilli, 1985; Paquet et al., 2007).

5.2. *Fault slip and dyke propagation from a magma chamber*

Fault slip profiles serve as indicators of the accumulated displacement occurring during the various phases of fault growth (Schlagenhauf et al., 2008), consistently also with hybrid models of normal fault growth, where fault evolution reflects the combined effects of segment linkage and along-strike propagation, rather than a single end-member growth mechanism (Rotevatn et al., 2019). When a normal fault grows symmetrically, it extends its tips in opposite directions, leading to an increase in length. At the same time, the vertical offset toward the center of the fault trace also increases, resulting in vertical growth (Tentler and Mazzoli, 2005). This process creates slip profiles which typically exhibit an elliptical shape (Pollard and Segall, 1987; Cowie and Scholz, 1992; Scholz, 2002). This is in contrast to an asymmetric slip profile, which results from a combination of vertical growth of the fault and unidirectional propagation of the slip plane (Nicol et al., 1996; Manighetti et al., 2001, 2004; Roche et al., 2012; Tibaldi et al., 2019). The relationship between fault slip distribution and asymmetric fault propagation was particularly analysed by Manighetti et al. (2001), who found that many slip profiles within the Afar Rift deviated from the symmetrical elliptical shape predicted by classical fault growth models. Instead, many profiles found in the Afar exhibited asymmetric, tapering geometries, reflecting the direction of fault propagation.

With reference to the slip profile shape of dyke-triggered faults, up to a few years ago there was a notable lack of data in the literature, particularly concerning fault tapering. Tibaldi et al. (2020c) described normal faults that gradually decrease in fault heave and finally transition into extension fractures, aligning with the direction of lateral dyke propagation during the Krafla Fires (1975–1984) in Iceland. This phenomenon appears to correspond to the tapering of graben faults in the same direction. A graben that formed during the 2014 Barðarbunga volcanotectonic event in Iceland, shows subsidence values that decrease to the north (Ruch et al., 2016). This decrease occurred in the same direction as the northward direction of lateral dyke propagation (Sigmundsson et al., 2015). Finally, fault slip profiles along the North-East Rift of Mt Etna, Italy, where compared with the contemporaneous shallow lateral injection of a dyke during the 1947 eruption (Tibaldi et al., 2025), demonstrating the consistency of the model of fault tapering in the same direction of dyke propagation. The same authors also carried out analogue physically-scaled experiments that arrived at the same result. In the same recent years, some research has begun to focus on systematically measuring fault slip profiles associated

with surface deformations triggered by dyke intrusions (Tibaldi et al., 2016, 2019, 2020b; Dumont et al., 2017). These studies indicate that normal faults typically taper outward from a magma chamber, which aligns with the direction of lateral dyke propagation. This has been explained as the effect of higher dyke accumulation closer to magma chambers, which induces a decrease of cumulated dyke thickness outwards from the chamber (Tibaldi et al., 2019; 2020b). Since surface deformation is proportional to dyke thickness, all other possible variables being equal, as a consequence slip at normal faults can decrease in the same direction.

Regarding our case study, the ASF, we analysed slip distributions along 150 main normal faults. Northward-tapering profiles were most common, comprising 44 % of the dataset and accounting for the largest cumulative fault length (Section 4.3; Fig. 15). These profiles are particularly abundant north of Hrúthálsar, supporting the interpretation of lateral dyke propagation from a magmatic source in that area. Our results are thus consistent with the observation that higher fault offsets near magma chambers likely reflect the cumulative effect of repeated dyke intrusions. Thus, a progressive reduction in slip magnitude is expected with increasing distance from these sources. Our data also highlight the presence of southward and northward tapering slip profiles between the Askja and the Hrúthálsar central volcanoes, reflecting the opposite directions of dyke propagation from the two magma chambers. Finally, a plausible explanation for the occurrence of northward-tapering slip profiles south of Askja, can be related to the presence of another active volcanic cluster further south. Below the Vatnajökull glacier in fact, there are several active volcanic centers, among which at least two, known as Grímsvötn and Bárðarbunga (Björnsson and Einarsson, 1990), are aligned with the AFS. Dykes emanated from a magma chamber below these glaciated centers may propagate northward along the AFS, triggering fault propagation in the same direction.

An alternative model to lateral dyke propagation within the Iceland rifts, suggests that dykes can ascend vertically to sub-vertically from an elongated reservoir at depth (e.g., Gudmundsson, 1984; Gudmundsson, 1995; Hartley and Thordarson, 2013 and references therein). This model may account for certain distal eruptions observed in the AFS, far from the central volcanoes. In such cases, the fault offset profiles may not reflect lateral propagation and are less likely to exhibit systematic tapering consistent with the injection direction. This may explain the occurrence of symmetric profiles and both northward- and southward-tapering profiles along the same graben structure. Finally, in theory some complication in fault-slip profile formation might arise in correspondence of the zone of interaction between a rift and a transform zone. Although fault tapering in this situation, as far as we know, has not been studied in the literature, in the area of crossing/interaction between the AFS and the Grímsey Lineament there are no faults. As a consequence, it is not possible to evaluate here the possible variations in fault kinematics and tapering in the proximity of a transform zone.

5.3. Structural reactivation and growth

The structures described in this work are well represented and readily detectable using orthomosaic and geomorphological data sets. Recent research and well-monitored intrusion and faulting events reveal that structures are commonly reactivated. The collapse of the Bárðarbunga caldera in 2014 (Gudmundsson et al., 2016) and dyke intrusion and eruptions that resulted in the Holuhraun lava fields were accompanied by widespread deformation and faulting. The structural analysis of data before and after these events suggests that both the eruption sites and the expression of accompanying normal faults were associated to reactivated structures (Hjartardóttir et al., 2016; Müller et al., 2017).

Similarly at the Reykjanes Peninsula (Iceland), during the 2021 dyke intrusion at Fagradalsfjall, repeated intrusions occurred with pre-existing structures having a large effect or even control on faulting (Glastonbury-Southern et al., 2025). Reactivation of structures may especially lead to strike-slip motions associated with dyke injections, with relevant surface features such as en-echelon and step-over structures (Glastonbury-Southern et al., 2025).

In this view, the structures identified, and inventory studied in our work may serve as a solid proxy for exploring potential sites of reactivations.

5.4. Interaction with transform zones

Stress accumulation between the NVZ and the Kolbeinsey Ridge is thought to have led to the formation of the Tjörnes Fracture Zone (Gudmundsson, 2007), which comprises three seismically active segments. The northernmost of these is the WNW-ESE-trending Grímsey Lineament, defined by a series of en-échelon NNW-striking, offshore grabens and normal faults. The dominant kinematics of this zone are characterised by normal faulting along NNW– to N–S-striking planes, with a subordinate strike-slip component (Rögnvaldsson et al., 1998; Lund and Townend, 2007). The Grímsey Lineament is normally mapped up to the Iceland coast (Fig. 1) at about 11 km west of the AFS.

At the Fremrinámar Fissure Swarm, immediately west of the AFS, the strike of the fracture swarm exhibits a marked anticlockwise rotation in correspondence of the Grímsey Lineament (Gudmundsson, 1993, 2007; Pedicini et al., 2023). Gudmundsson (2007) attributed this rotation to the interaction between the Fremrinámar Fissure Swarm and the Kolbeinsey Ridge during the northward propagation of the former. This interaction is hypothesised to have contributed to the formation of the Grímsey Lineament, representing an early stage in the development of a mature strike-slip system, such as the Húsavík–Flatey Fault.

Within the northern AFS, our dataset shows a general NNW–SSE structural trend in proximity to the Grímsey Lineament (e.g. Figs. 4 and 15). North of this area, fracture intensity, rift width, and dilation values show a pronounced decrease, accompanied by generally lower fault vertical offsets. All these observations suggest that the AFS may also be undergoing interaction with the Kolbeinsey Ridge through the Grimesy Lineament, which might be hidden here below the Holocene deposits.

Another possible interaction between the structures of the AFS and a transversal main mechanical boundary, can be represented by the discontinuities coinciding with the trace of the Jökulsá á Fjöllum River (e.g. Fig. 15), the second longest river in Iceland. This river originates from the Vatnajökull Glacier and traverses the entire NVZ before reaching the Atlantic Ocean to the north, with a general NNW trend (Fig. 3). Analysis of rock unit age distribution within the AFS, reveals that this river marks a significant geological boundary; north of the Jökulsá á Fjöllum, the exposed units are predominantly pre-LGM in age, whereas the central and southern sectors (south of the river) are dominated by post-LGM deposits. This spatial distinction was previously noted by Sæmundsson (1974), who reported that the youngest volcanic units and central volcanoes within the NVZ are generally located southwest of the river, while the northeastern side is characterised by older lithologies and an absence of central volcanoes.

In our dataset, at the latitude of the Jökulsá á Fjöllum, we also identify a sharp reduction in fracture intensity and rift width. This behaviour may be attributed to: i) the presence of surficial deposits concealing underlying fractures, or ii) the existence of an underlying tectonic structure—possibly a buried transform fault—that induces a change in the behaviour and geometry of the fracture swarm. It is plausible that the accumulation of surficial material in this region reflects a topographic depression associated with such a buried structural feature. Furthermore, both extension fractures and eruptive fissures exhibit a marked decline in frequency north of the river. An interpretation that favours the presence of an underlying tectonic structure is also linked to the observation that the course of the Jökulsá á Fjöllum River itself is composed of several segments with variable orientations, shifting several times with sharp angles from a N–S trend to NW–SE segments. These are typical characteristics of a tectonic-controlled river course. While the principal azimuth of the AFS ranges from N–S to

NNE–SSW, NNW–SSE-trending structures are also locally present at the intersection with the river. Also other structural changes have been individuated at the latitude of the river, including the local reduction in fault frequency, dilation, extension fractures and eruptive fissures, suggesting that a discontinuity along the Jökulsá á Fjöllum River acts as a localised barrier to deformation.

5.5. Propagation of the Askja rift

We finally explored the hypothesis of a northward propagation of NVZ's extension, i.e. towards the Kolbeinsey Ridge (Sæmundsson, 1979; Schilling et al., 1982; Hardarson et al., 1997; Harðarson et al., 2008; Einarsson, 2008). Stress accumulation between these segments of the Mid-Atlantic Ridge has driven the development of the Tjörnes Fracture Zone and the reorientation of the NVZ's northeastern margin towards Kolbeinsey (Gudmundsson, 1993, 2007). This northward propagation is interpreted as a response to the outward migration of tectonic deformation away from the Icelandic hotspot (Ito, 2001; Hey et al., 2010), located beneath the Vatnajökull Glacier, marking the southern limit of the NVZ. This deformation pattern has produced a wedge-shaped geometry in the rift zone (Karson, 2017).

On our dataset, we observed that, immediately south of the Jökulsá á Fjöllum River, extension fractures become more prevalent, particularly in proximity to the Hrúthálsar volcanic edifice. These features are often regarded as indicative of early-stage rift development (Corti et al., 2021), based on the concept that normal faults evolve from extension fractures once a critical depth is reached, enabling shear displacement (Gudmundsson, 1992). The clustering of extension fractures near Hrúthálsar and just south of the river suggests that the most recent deformation within the AFS is currently concentrated in this region. Also, the general decrease of faults and eruptive fissures northward, can be a further indication of lower maturity of the rift in the same direction. Similarly, most Holocene products have been emitted in the central and southern portion of the AFS, further sustaining the northward propagation hypothesis. Finally, fault-slip profile analysis further supports this interpretation, revealing a predominance of northward-tapering profiles, also indicative of a general northward rift propagation.

The AFS not only presents a northward asymmetry, but it also shows some longitudinal differences. All the structures analysed along the rift in fact, have an asymmetric distribution, with the longer structures more developed towards the east. This includes the W- and E-dipping faults and the extension fractures, whereas the eruptive fissures are more symmetric. We can speculate that this asymmetry derives from a higher maturity of the eastern side of the rift, which is expanding its width in the opposite direction.

6. Conclusions

We mapped at 1:50,000 scale, all the Holocene structures of the Askja Fissure Swarm (AFS), in the Northern Volcanic Zone of Iceland, through the interpretation of aerial photos, orthomosaics, Digital Surface Models, and virtual field checks. A total of 3749 structures have been analysed, including the measurement of their strike, dip, length and kinematics. Here the main issues:

- We recognized 395 eruptive fissures, 2301 extension dry fractures (fissures), and 1038 normal faults, of which 536 dip eastward and 502 westward. The overall dataset exhibits a predominant N–S to NNE–SSW strike, with an average strike of N17.5°E. Structure lengths vary from 10 m to 13,380 m, with a mean of 445 m. Normal faults are generally longer than other structures, with a mean of 1042 m.
- The majority of eruptive fissures are concentrated in correspondence of the Askja and Hrúthálsar central volcanoes. Outward from these volcanoes, fault length and offset, and number of extension fractures and of faults decrease with distance.
- Along the main faults (length >2 km), we reconstructed the slip profiles, with the aim of evaluating the direction of along-axis rift propagation. Fault slip profiles taper outward from the Askja and Hrúthálsar volcanoes.
- We interpret all these characteristics as the effect of multiple dykes that laterally propagated outward from the magma chambers below Askja and Hrúthálsar central volcanoes. Dykes decrease in number and thickness outward from the source region, thus explaining the decrease of dyke-triggered shallow deformation. This process highlights the importance of magma-related stresses in shaping a rift zone.
- We also observed variation of fracture intensity and strike where the AFS intersects the Jökulsá á Fjöllum River and the possible prolongation of the Grimsey Lineament, here interpreted as locations of possible hidden inherited transversal structures.
- Looking at the whole AFS, the tapering of fault slip profiles shows a dominant northward propagation of faults tapering. This may indicate the superimposition of a regional northward propagation of the rift on the local effects of dykes and magma chambers.

We believe that the reconstruction of fault-slip profiles along an active rift, coupled with a detailed characterization of all the structures, can reveal critical information about the cause, orientation and progression of extensional deformation. These data were instrumental here in assessing both the northward propagation of the rift and the superimposition of local magmatic processes on regional tectonics to shape rift dynamics.

CRediT authorship contribution statement

Fabio Luca Bonali: Writing – original draft, Supervision, Conceptualization. **Martina Pedicini:** Writing – original draft, Methodology, Investigation. **Thomas R. Walter:** Writing – review & editing, Supervision. **Alessandro Tibaldi:** Writing – original draft, Supervision.

Declaration of competing interest

The authors declare that they have no known competing financial interests or personal relationships that could have appeared to influence the work reported in this paper.

Acknowledgments

This work was supported by the Doctoral School of Chemical, Geological and Environmental Sciences (Milano Bicocca) funding (2018-CONT-0157). The work was carried out under the framework of the CRUST - Interuniversity Centre for 3D Seismotectonics with Territorial Applications, and under the aegis of the International Lithosphere Program, Task Force II. This manuscript is also an outcome of the Virtual Reality Lab for Earth Sciences - GeoVires (https://geovires.unimib.it/), University of Milano Bicocca; Agisoft Metashape is acknowledged for photogrammetry processing. We thank two anonymous reviewers for their constructive comments, which improved the manuscript, and the editor, M. Irene B. Raposo.

Data availability

Data will be made available on request.

References

Acocella, V., Neri, M., 2009. Dike propagation in volcanic edifices: overview and possible developments. Tectonophysics 471 (1–2), 67–77.
Acocella, V., Trippanera, D., 2016. How diking affects the tectonomagmatic evolution of slow spreading plate boundaries: overview and model. Geosphere 12 (3), 867–883.

Ágústsdóttir, T., Woods, J., Greenfield, T., Green, R.G., White, R.S., Winder, T., et al., 2016. Strike-slip faulting during the 2014 Bárðarbunga-Holuhraun dike intrusion, central Iceland. Geophys. Res. Lett. 43 (4), 1495–1503.
Andrew, R.E., Gudmundsson, A., 2008. Volcanoes as elastic inclusions: their effects on the propagation of dykes, volcanic fissures, and volcanic zones in Iceland. J. Volcanol. Geoth. Res. 177 (4), 1045–1054.
Antoniou, V., Bonali, F.L., Nomikou, P., Tibaldi, A., Melissinos, P., Mariotto, F.P., et al., 2020. Integrating virtual reality and GIS tools for geological mapping, data collection and analysis: an example from the Metaxa Mine, Santorini (Greece). Appl. Sci. 10 (23), 8317.
Árnadóttir, T., Lund, B., Jiang, W., Geirsson, H., Björnsson, H., Einarsson, P., Sigurdsson, T., 2009. Glacial rebound and plate spreading: results from the first countrywide GPS observations in Iceland. Geophys. J. Int. 177 (2), 691–716.
Björnsson, H., Einarsson, P., 1990. Volcanoes beneath Vatnajökull, Iceland: evidence from radio echo-sounding, earthquakes and jökulhlaups. Jokull (40), 147–168.
Björnsson, A., 1985. Dynamics of crustal rifting in NE Iceland. J. Geophys. Res. Solid Earth 90 (B12), 10151–10162.
Björnsson, A., Johnsen, G., Sigurdsson, S., Thorbergsson, G., Tryggvason, E., 1979. Rifting of the plate boundary in North Iceland 1975–1978. J. Geophys. Res. Solid Earth 84 (B6), 3029–3038.
Bonali, F.L., Tibaldi, A., Marchese, F., Fallati, L., Russo, E., Corselli, C., Savini, A., 2019a. UAV-based surveying in volcano-tectonics: an example from the Iceland rift. J. Struct. Geol. 121, 46–64.
Bonali, F.L., Tibaldi, A., Mariotto, F.P., Saviano, D., Meloni, A., Sajovitz, P., 2019b. Geometry, oblique kinematics and extensional strain variation along a diverging plate boundary: the example of the northern Theistareykir Fissure Swarm, NE Iceland. Tectonophysics 756, 57–72.
Bonali, F.L., Corti, N., Mariotto, F.P., De Beni, E., Bressan, S., Cantarero, M., et al., 2024a. 3D study of dyke-induced asymmetric graben: the 1971 Mt. Etna (Italy) case by structural data and numerical modelling. J. Struct. Geol. 187, 105231.
Bonali, F.L., Vitello, F., Kearl, M., Tibaldi, A., Whitworth, M., Antoniou, V., et al., 2024b. GeaVR: an open-source tools package for geological-structural exploration and data collection using immersive virtual reality. Appl. Comput. Geosci. 21, 100156.
Brandsdóttir, B., Einarsson, P., 1979. Seismic activity associated with the September 1977 deflation of the Krafla central volcano in northeastern Iceland. J. Volcanol. Geoth. Res. 6 (3–4), 197–212.
Brown, G.C., Everett, S.P., Rymer, H., McGarvie, D.W., Foster, I., 1991. New light on caldera evolution—Askja, Iceland. Geology 19 (4), 352–355.
Buck, W.R., Einarsson, P., Brandsdóttir, B., 2006. Tectonic stress and magma chamber size as controls on dike propagation: constraints from the 1975–1984 Krafla rifting episode. J. Geophys. Res. Solid Earth 111 (B12).
Bürgmann, R., Pollard, D.D., Martel, S.J., 1994. Slip distributions on faults: effects of stress gradients, inelastic deformation, heterogeneous host-rock stiffness, and fault interaction. J. Struct. Geol. 16 (12), 1675–1690.
Carbotte, S., Welch, S.M., Macdonald, K.C., 1991. Spreading rates, rift propagation, and fracture zone offset histories during the past 5 my on the Mid-Atlantic Ridge; 25–27 30′ S and 31–34 30′ S. Mar. Geophys. Res. 13, 51–80.
Cooper, P.A., Milholland, P.D., Duennebier, F.K., 1987. Seismicity of the Galapagos 95.5W propagating rift. J. Geophys. Res. Solid Earth 92 (B13), 14091–14112.
Corti, G., Bonini, M., Conticelli, S., Innocenti, F., Manetti, P., Sokoutis, D., 2003. Analogue modelling of continental extension: a review focused on the relations between the patterns of deformation and the presence of magma. Earth Sci. Rev. 63 (3–4), 169–247.
Corti, N., Bonali, F.L., Russo, E., Drymoni, K., Mariotto, F.P., Gudmundsson, A., Esposito, R., Cavallo, A., Tibaldi, A., 2023. Feeders vs arrested dikes: a case study from the Younger Stampar eruption in Iceland. J. Volcanol. Geoth. Res. 443, 107914.
Corti, N., Bonali, F.L., Pasquaré Mariotto, F., Tibaldi, A., Russo, E., Hjartardottir, A.R., Einarsson, P., Rigoni, V., Bressan, S., 2021. Fracture kinematics and holocene stress field at the Krafla rift, northern Iceland. Geosciences 11 (2), 101.
Costantini, M., Minati, F., Trillo, F., Ferretti, A., Novali, F., Passera, E., Andersen, H.S., 2021. European ground motion service (EGMS). In: *2021 IEEE international geoscience and remote sensing symposium IGARSS*. IEEE, pp. 3293–3296.
Cowie, P.A., Scholz, C.H., 1992. Growth of faults by accumulation of seismic slip. J. Geophys. Res. Solid Earth 97 (B7), 11085–11095.
De Pascale, G.P., Fischer, T.J., Moreland, W.M., Geirsson, H., Hrubcová, P., Drouin, V., et al., 2024. On the move: 2023 observations on real time graben formation, Grindavík, Iceland. Geophys. Res. Lett. 51 (14) e2024GL110150.
Døssing, A., Kolster, M.E., da Silva, E.L., Muxworthy, A.R., Petersen, J.T., Riishuus, M.S., 2024. Pre-existing structural control on the recent Holuhraun eruptions along the Bárðarbunga spreading center, Iceland. Sci. Rep. 14 (1), 3399.
Ducrocq, C., Árnadóttir, T., Einarsson, P., Jónsson, S., Drouin, V., Geirsson, H., Hjartardóttir, Á.R., 2024. Widespread fracture movements during a volcano-tectonic unrest: the Reykjanes Peninsula, Iceland, from 2019–2021 TerraSAR-X interferometry. Bull. Volcanol. 86 (2), 14.
Dumont, S., Klinger, Y., Socquet, A., Doubre, C., Jacques, E., 2017. Magma influence on propagation of normal faults: evidence from cumulative slip profiles along Dabbahu-Manda-Hararo rift segment (Afar, Ethiopia). J. Struct. Geol. 95, 48–59.
Einarsson, P., 1991. Earthquakes and present-day tectonism in Iceland. Tectonophysics 189 (1–4), 261–279.
Einarsson, P., 2008. Plate boundaries, rifts and transforms in Iceland. Jökull 58, 35–58.
Einarsson, P., Brandsdottir, B., 1980. Seismological evidence for lateral magma intrusion during the July 1978 deflation of the Krafla volcano in NE-Iceland. J. Geophys. 47 (1), 160–165.
Einarsson, P., Brandsdóttir, B., 2021. Seismicity of the Northern volcanic zone of Iceland. Front. Earth Sci. 9, 628967.
Forslund, T., Gudmundsson, A., 1991. Crustal spreading due to dikes and faults in southwest Iceland. J. Struct. Geol. 13 (4), 443–457.
Franke, D., Jokat, W., Ladage, S., Stollhofen, H., Klimke, J., Lutz, R., et al., 2015. The offshore East African Rift system: structural framework at the toe of a juvenile rift. Tectonics 34 (10), 2086–2104.
Gerloni, I.G., Carchiolo, V., Vitello, F.R., Sciacca, E., Becciani, U., Costa, A., Tibaldi, A., 2018, September. Immersive virtual reality for earth sciences. In: *Federated conference on computer science and information systems (FedCSIS)*. IEEE, pp. 527–534.
Glastonbury-Southern, E., Winder, T., Rawlinson, N., White, R.S., Greenfield, T., Bacon, C.A., et al., 2025. Pre-existing structures control the orientation of strike-slip faulting during the 2021 dike intrusion at Fagradalsfjall, Iceland. J. Geophys. Res. Solid Earth 130 (6) e2024JB030162.
Gray, T.G., 1992. Handbook of Crack Opening Data: a Compendium of Equations, Graphs, Computer Software and References for Opening Profiles of Cracks in Loaded Components and Structures. Elsevier.
Gudmundsson, A., 1983. Form and dimensions of dykes in eastern Iceland. Tectonophysics 95, 295–307.
Gudmundsson, A., 1984. Formation of dykes, feeder-dykes, and the intrusion of dykes from magma chambers. Bull. Volcanol. 47 (3), 537–550.
Gudmundsson, A., 1988. Formation of collapse calderas. Geology 16 (9), 808–810.
Gudmundsson, A., 1992. Formation and growth of normal faults at the divergent plate boundary in Iceland. Terra Nova 4 (4), 464–471.
Gudmundsson, A., 1993. On the structure and formation of fracture zones. Terra Nova 5 (3), 215–224.
Gudmundsson, A., 1995. Infrastructure and mechanics of volcanic systems in Iceland. J. Volcanol. Geoth. Res. 64, 1–22.
Gudmundsson, A., 2000. Dynamics of volcanic systems in Iceland: example of tectonism and volcanism at juxtaposed hot spot and mid-ocean ridge systems. Annu. Rev. Earth Planet Sci. 28, 107–140.
Gudmundsson, A., 2003. Surface stresses associated with arrested dykes in rift zones. Bull. Volcanol. 65, 606–619.
Gudmundsson, A., 2007. Infrastructure and evolution of ocean-ridge discontinuities in Iceland. J. Geodyn. 43 (1), 6–29.
Gudmundsson, A., 2011. Rock Fractures in Geological Processes. Cambridge University Press.
Gudmundsson, A., 2020. *Volcanotectonics: Understanding the structure, deformation and dynamics of volcanoes*. Cambridge University Press.
Gudmundsson, M.T., Jónsdóttir, K., Hooper, A., Holohan, E.P., Halldórsson, S.A., Ófeigsson, B.G., et al., 2016. Gradual caldera collapse at Bárdarbunga volcano, Iceland, regulated by lateral magma outflow. Science 353 (6296) aaf8988.
Hardarson, B.S., Fitton, J.G., Ellam, R.M., Pringle, M.S., 1997. Rift relocation—a geochemical and geochronological investigation of a palaeo-rift in northwest Iceland. Earth and Planetary Science Letters 153 (3–4), 181–196.
Harðarson, B.S., Fitton, J.G., Hjartarson, Á., 2008. Tertiary volcanism in Iceland. Jökull 58, 161–178.
Harknett, J., Whitworth, M., Rust, D., Krokos, M., Kearl, M., Tibaldi, A., et al., 2022. The use of immersive virtual reality for teaching fieldwork skills in complex structural terrains. J. Struct. Geol. 163, 104681.
Hartley, M.E., Thordarson, T., 2012. Formation of Öskjuvatn caldera at Askja, North Iceland: mechanism of caldera collapse and implications for the lateral flow hypothesis. J. Volcanol. Geoth. Res. 227, 85–101.
Hartley, M.E., Thordarson, T., 2013. The 1874–1876 volcano-tectonic episode at Askja, North Iceland: lateral flow revisited. G-cubed 14 (7), 2286–2309.
Helgason, J., Zentilli, M., 1985. Field characteristics of laterally emplaced dikes: anatomy of an exhumed Miocene dike swarm in Reydarfjördur, eastern Iceland. Tectonophysics 115, 247–274. https://doi.org/10.1016/0040-1951(85)90141-6.
Hey, R., Martinez, F., Höskuldsson, Á., Benediktsdóttir, Á., 2010. Propagating rift model for the V-shaped ridges south of Iceland. G-cubed 11 (3).
Hjartardóttir, Á.R., Einarsson, P., 2015. The interaction of fissure swarms and monogenetic lava shields in the rift zones of Iceland. J. Volcanol. Geoth. Res. 299, 91–102.
Hjartardóttir, Á.R., Einarsson, P., 2021. Tectonic position, structure, and Holocene activity of the Hofsjökull volcanic system, central Iceland. J. Volcanol. Geoth. Res. 417, 107277.
Hjartardóttir, Á.R., Einarsson, P., Gudmundsson, M.T., Högnadóttir, T., 2016a. Fracture movements and graben subsidence during the 2014 Bárðarbunga dike intrusion in Iceland. J. Volcanol. Geoth. Res. 310, 242–252.
Hjartardóttir, Á.R., Einarsson, P., Magnúsdóttir, S., Björnsdóttir, Þ., Brandsdóttir, B., 2016b. Fracture systems of the Northern Volcanic Rift Zone, Iceland: an onshore part of the Mid-Atlantic plate boundary. Geological Society, London, Special Publications 420 (1), 297–314.
Hjartarson, A., Sæmundsson, K., 2014. Bedrock Map of Iceland 1: 600 000. Iceland GeoSurvey.
Hollingsworth, J., Leprince, S., Ayoub, F., Avouac, J.P., 2013. New constraints on dike injection and fault slip during the 1975–1984 Krafla rift crisis, NE Iceland. J. Geophys. Res. Solid Earth 118 (7), 3707–3727.
Hollingsworth, J., Leprince, S., Ayoub, F., Avouac, J.P., 2012. Deformation during the 1975–1984 Krafla rifting crisis, NE Iceland, measured from historical optical imagery. J. Geophys. Res. Solid Earth 117, 3707–3727.
Ito, G., 2001. Reykjanes' V'-shaped ridges originating from a pulsing and dehydrating mantle plume. Nature 411 (6838), 681–684.
Jacques, E., Ruegg, J.C., Lepine, J.C., Tapponnier, P., King, G.C.P., Omar, A., 1999. Relocation of M≥2 events of the 1989 Dobi seismic sequence in Afar: evidence for earthquake migration. Geophys. J. Int. 138 (2), 447–469.
Karson, J.A., 2017. The Iceland plate boundary zone: propagating rifts, migrating transforms, and rift-parallel strike-slip faults. G-cubed 18 (11), 4043–4054.

Keir, D., Ebinger, C.J., Stuart, G.W., Daly, E., Ayele, A., 2006. Strain accommodation by magmatism and faulting as rifting proceeds to breakup: seismicity of the northern Ethiopian rift. J. Geophys. Res. Solid Earth 111 (B5).
Koehn, D., Aanyu, K., Haines, S., Sachau, T., 2008. Rift nucleation, rift propagation and the creation of basement micro-plates within active rifts. Tectonophysics 458 (1–4), 105–116.
Koopmann, H., Brune, S., Franke, D., Breuer, S., 2014. Linking rift propagation barriers to excess magmatism at volcanic rifted margins. Geology 42 (12), 1071–1074.
Lund, B., Townend, J., 2007. Calculating horizontal stress orientations with full or partial knowledge of the tectonic stress tensor. Geophys. J. Int. 170 (3), 1328–1335.
Macdonald, R., Sparks, R.S.J., Sigurdsson, H., Mattey, D.P., McGarvie, D.W., Smith, R.L., 1987. The 1875 eruption of Askja volcano, Iceland: combined fractional crystallization and selective contamination in the generation of rhyolitic magma. Mineral. Mag. 51 (360), 183–202.
Macheyeki, A.S., Macheyeki, M.A., 2025. Morphostructural analysis of the Eyasi–Durumo-Manyara-faults, East African Rift System. J. Geol. Soc. India 101 (5), 685–693.
Manighetti, I., King, G., Sammis, C.G., 2004. The role of off-fault damage in the evolution of normal faults. Earth Planet Sci. Lett. 217 (3–4), 399–408.
Manighetti, I., King, G.C.P., Gaudemer, Y., Scholz, C.H., Doubre, C., 2001. Slip accumulation and lateral propagation of active normal faults in Afar. J. Geophys. Res. Solid Earth 106 (B7), 13667–13696.
Mart, Y., Dauteuil, O., 2000. Analogue experiments of propagation of oblique rifts. Tectonophysics 316 (1–2), 121–132.
McClay, K.R., White, M.J., 1995. Analogue modelling of orthogonal and oblique rifting. Mar. Petrol. Geol. 12 (2), 137–151.
Metzger, S., Jonsson, S., 2014. Plate boundary deformation in North Iceland during 1992–2009 revealed by InSAR time-series analysis and GPS. Tectonophysics 634, 127–138.
Morgan, W.J., 1972. Deep mantle convection plumes and plate motions. AAPG Bull. 56 (2), 203–213.
Müller, D., Walter, T.R., Schöpa, A., Witt, T., Steinke, B., Gudmundsson, M.T., Dürig, T., 2017. High-resolution digital elevation modeling from TLS and UAV campaign reveals structural complexity at the 2014/2015 Holuhraun eruption site, Iceland. Front. Earth Sci. 5, 59.
Nicol, A., Watterson, J., Walsh, J.J., Childs, C., 1996. The shapes, major axis orientations and displacement patterns of fault surfaces. J. Struct. Geol. 18 (2–3), 235–248.
Panza, E., Ruch, J., Oestreicher, N., 2024. Rift obliquity in the Northern Volcanic Zone in Iceland using UAV-based structural data. J. Volcanol. Geoth. Res. 450, 108072.
Paquet, F., Dauteuil, O., Hallot, E., Moreau, F., 2007. Tectonics and magma dynamics coupling in a dyke swarm of Iceland. J. Struct. Geol. 29, 1477–1493. https://doi.org/10.1016/j.jsg.2007.06.001.
Parks, M.M., Heimisson, E.R., Sigmundsson, F., Hooper, A., Vogfjörd, K.S., Árnadóttir, T., Ólafsdóttir, R., 2017. Evolution of deformation and stress changes during the caldera collapse and dyking at Bárdarbunga, 2014–2015: Implication for triggering of seismicity at nearby Tungnafellsjökull volcano. Earth and Planetary Science Letters 462, 212–223.
Parmentier, E.M., Schubert, G., 1989. Rift propagation. Geophys. Res. Lett. 16 (2), 183–186.
Peacock, D.C.P., Sanderson, D.J., 1991. Displacements, segment linkage and relay ramps in normal fault zones. J. Struct. Geol. 13 (6), 721–733.
Pedicini, M., Bonali, F.L., Corti, N., Tibaldi, A., 2025. Rift structure and development: the Krafla Fissure Swarm (Northern Iceland). J. Struct. Geol. 191, 105332.
Pedicini, M., Bonali, F.L., Corti, N., Pasquaré Mariotto, F.A., Drymoni, K., Tibaldi, A., 2023. A step forward to understanding the development of volcanotectonic rifts: the structure of the Fremrinamar Fissure Swarm (Iceland). Front. Earth Sci. 11, 1271721.
Pollard, D.D., Delaney, P.T., Duffield, W.A., Endo, E.T., Okamura, A.T., 1983. Surface deformation involcanic rift zones. Tectonophysics 94, 541–584.
Pollard, D.D., Segall, P., 1987. Theoretical displacements and stresses near fractures in rock: with applications to faults, joints, veins, dikes and solution surfaces. In: Atkinson, B.K. (Ed.), Fracture Mechanics of Rock. American Press Inc., London, pp. 277–349.
Porter, C., Howat, I., Noh, M., Husby, E., Khuvis, S., Danish, E., Tomko, K., Gardiner, J., Negrete, A., Yadav, B., Klassen, J., Kelleher, C., Cloutier, M., Bakker, J., Enos, J., Arnold, G., Bauer, G., Morin, P., 2023. "ArcticDEM - strips. Harvard Dataverse. https://doi.org/10.7910/DVN/C98DVS, Version 4.1. . (Accessed 27 June 2024).
Porter, C., Morin, P., Howat, I., Noh, M., Bates, B., Peterman, K., Keesey, S., Schlenk, M., Gardiner, J., Tomko, K., Willis, M., Kelleher, C., Cloutier, M., Husby, E., Foga, S., Nakamura, H., Platson, M., Wethington, M., Williamson, C., Bauer, G., Enos, J., Arnold, G., Kramer, W., Becker, P., Doshi, A., D'Souza, C., Cummens, P., Laurier, F., Bojesen, M., 2018. ArcticDEM, Version 3. Harvard Dataverse. https://doi.org/10.7910/DVN/OHHUKH. (Accessed 27 April 2022).
Roche, V., Homberg, C., Rocher, M., 2012. Fault displacement profiles in multilayer systems: from fault restriction to fault propagation. Terra Nova 24 (6), 499–504.
Rögnvaldsson, S.T., Gudmundsson, Á., Slunga, R., 1998. Seismotectonic analysis of the Tjörnes Fracture Zone, an active transform fault in north Iceland. J. Geophys. Res. Solid Earth 103 (B12), 30117–30129.
Rotevatn, A., Jackson, C.A.L., Tvedt, A.B., Bell, R.E., Blækkan, I., 2019. How do normal faults grow? J. Struct. Geol. 125, 174–184.
Rubin, A.M., Pollard, D.D., 1988. Dike-induced faulting in rift zones of Iceland and Afar. Geology 16 (5), 413–417.
Rubin, A.M., 1992. Dike-induced faulting and graben subsidence in volcanic rift zones. J. Geophys. Res. Solid Earth 97 (B2), 1839–1858.
Ruch, J., Wang, T., Xu, W., Hensch, M., Jónsson, S., 2016. Oblique rift opening revealed by reoccurring magma injection in central Iceland. Nat. Commun. 7, 12352.
Ruz, J., Browning, J., Cembrano, J., Iturrieta, P., Gerbault, M., Sielfeld, G., 2020. Field observations and numerical models of a Pleistocene-Holocene feeder dyke swarm associated with a fissure complex to the east of the Tatara-San Pedro-Pellado complex, Southern Volcanic Zone, Chile. J. Volcanol. Geoth. Res. 404, 107033.
Sæmundsson, K., 1974. Evolution of the axial rifting zone on Northern Iceland and the Tjörnes Fracture Zone. Geol. Soc. Am. Bull. 85, 495–504.
Sæmundsson, K., 1977. Geological map of Iceland. Sheet 7, North East Iceland. Iceland Geodetic Survey and the Museum of Natural History.
Sæmundsson, K., Hjartarson, Á., Kaldal, I., Sigurgeirsson, M.Á., Kristinsson, S.G., Víkingsson, S., 2012. Geological map of the Northern Volcanic Zone, Iceland. Northern part. 000. Reykjavík: Iceland GeoSurvey and Landsvirkjun 1, 100.
Sæmundsson, K., Jóhannesson, H., Grönvold, K., 2005. Hrúthálsar, a central volcano in Ódáðahraun. Spring Conference of the Icelandic Geological Society. The Icelandic Geological Society, Reykjavík (in Icelandic).
Sæmundsson, K., 1979. Outline of the geology of Iceland. Jokull 29, 7–28.
Schilling, J.G., Meyer, P.S., Kingsley, R.H., 1982. Evolution of the Iceland hotspot. Nature 296 (5855), 313–320.
Schlagenhauf, A., Manighetti, I., Malavieille, J., Dominguez, S., 2008. Incremental growth of normal faults: insights from a laser-equipped analog experiment. Earth Planet Sci. Lett. 273, 299–311. https://doi.org/10.1016/j.epsl.2008.06.042.
Scholz, C.H., 2002. The Mechanics of Earthquakes and Faulting. Cambridge University Press.
Schonberger, J.L., Frahm, J.M., 2016. Structure-from-motion revisited. In: Proceedings of the IEEE Conference on Computer Vision and Pattern Recognition, pp. 4104–4113.
Schouten, H., Dick, H.J., Klitgord, K.D., 1987. Migration of mid-ocean-ridge volcanic segments. Nature 326 (6116), 835–839.
Sigmundsson, F., Einarsson, P., Hjartardóttir, Á.R., Drouin, V., Jónsdóttir, K., Arnadottir, T., et al., 2020. Geodynamics of Iceland and the signatures of plate spreading. J. Volcanol. Geoth. Res. 391, 106436.
Sigmundsson, F., Hooper, A., Hreinsdottir, S., Vogfjord, K.S., Ofeigsson, B.G., Heimisson, E.R., Dumont, S., Parks, M., Spaans, K., Gudmundsson, G.B., Drouin, V., Árnadottir, T., Jonsdóttir, K., Gudmundsson, M.T., Hognadottir, T., Fridriksdóttir, H. M., Hensch, M., Einarsson, P., Magnússon, E., Samsonov, S., Brandsdottir, B., White, R.S., Agústsdottir, T., Greenfield, T., Green, R.G., Hjartardottir, A.R., Pedersen, R., Bennett, R.A., Geirsson, H., La Femina, P.C., Bjornsson, H., Palsson, F., Sturkell, E., Bean, C.J., Mollhoff, M., Braiden, A.K., Eibl, E.P.S., 2015. Segmented lateral dyke growth in a rifting event at B arðarbunga volcanic system, Iceland. Nature 517 (7533), 191–195.
Sigurdsson, H., Sparks, R.S.J., 1978. Rifting episode in north Iceland in 1874–1875 and the eruptions of Askja and Sveinagja. Bull. Volcanol. 41, 149–167.
Sigurdsson, O., 1980. Surface deformation of the Krafla fissure swarm in two rifting events. J. Geophys. 47 (1), 154–159.
Sigurgeirsson, M.Á., Hjartarson, Á., Kaldal, I., Sæmundsson, K., Kristinsson, S.G., Víkingsson, S., 2015. Geological Map of the Northern Volcanic Zone, Iceland. Southern Part, 1:100,000. Reykjavík: Iceland GeoSurvey.
Sigvaldason, G.E., 2002. Volcanic and tectonic processes coinciding with glaciation and crustal rebound: an early Holocene rhyolitic eruption in the Dyngjufjöll volcanic centre and the formation of the Askja caldera, north Iceland. Bull. Volcanol. 64, 192–205.
Sneddon, I.N., Lowengrub, M., 1969. Crack Problems in the Classical Theory of Elasticity. Wiley, NewYork.
Stal, C., Bourgeois, J., De Maeyer, P., De Mulder, G., De Wulf, A., Goossens, R., et al., 2012. Test case on the quality analysis of structure from motion in airborne applications. In: 32nd EARSeL Symposium: Advances in Geosciences. European Association of Remote Sensing Laboratories (EARSeL).
Sturkell, E., Sigmundsson, F., 2000. Continuous deflation of the Askja caldera, Iceland, during the 1983–1998 non-eruptive period. J. Geophys. Res. Solid Earth 105 (B11), 25671–25684.
Tentler, T., Mazzoli, S., 2005. Architecture of normal faults in the rift zone of central north Iceland. J. Struct. Geol. 27, 1721–1739.
Tibaldi, A., 2015. Structure of volcano plumbing systems: a review of multi-parametric effects. J. Volcanol. Geoth. Res. 298, 85–135.
Tibaldi, A., Bonali, F.L., 2017. Intra-arc and back-arc volcano-tectonics: magma pathways at Holocene Alaska-Aleutian volcanoes. Earth Sci. Rev. 167, 1–26.
Tibaldi, A., Bonali, F.L., Pasquaré, F.A., Rust, D., Cavallo, A., D`urso, A., 2013. Structure of regional dykes and local cone sheets in the Midhyrna-Lysuskard area, Snaefellsnes Peninsula (NW Iceland). Bull. Volcanol. 75 (11), 764.
Tibaldi, A., Bonali, F.L., Pasquarè Mariotto, F., Russo, E., Tenti, L.R., 2019. The development of divergent margins: insights from the North volcanic zone, Iceland. Earth Planet Sci. Lett. 509, 1–8.
Tibaldi, A., Bonali, F.L., Einarsson, P., Hjartardóttir, Á.R., Mariotto, F.P., 2016. Partitioning of Holocene kinematics and interaction between the Theistareykir Fissure Swarm and the Husavik-Flatey fault, North Iceland. Journal of Structural Geology 83, 134–155.
Tibaldi, A., Bonali, F.L., Pasquaré Mariotto, F., Corti, N., Russo, E., Einarsson, P., Hjartardottir, A.R., 2020a. Rifting kinematics produced by magmatic and tectonic stresses in the north volcanic zone of Iceland. Front. Earth Sci. 8, 174.
Tibaldi, A., Corti, N., Bonali, F.L., Mariotto, F.P., Russo, E., 2020b. Along-rift propagation of Pleistocene-Holocene faults from a central volcano. J. Struct. Geol. 141, 104201.
Tibaldi, A., Bonali, F.L., Russo, E., Fallati, L., 2020c. Surface deformation and strike-slip faulting controlled by dyking and host rock lithology: a compendium from the Krafla Rift, Iceland. J. Volcanol. Geoth. Res., 106835
Tibaldi, A., Luppino, A., De Beni, E., Corti, N., Cantarero, M., Mariotto, F.P., Bonali, F.L., 2025. Effects of lateral dyke propagation and pre-existing fractures on shallow deformation: Data from the Etna 1947 eruption and analogue models. Journal of Volcanology and Geothermal Research, 108349.

Tibaldi, A., 1995. Morphology of pyroclastic cones and tectonics. Journal of Geophysical Research: Solid Earth 100 (B12), 24521–24535.
Tibaldi, A., Pasquare, F.A., Papanikolaou, D., Nomikou, P., 2008. Tectonics of Nisyros Island, Greece, by field and offshore data, and analogue modelling. J. Struct. Geol. 30 (12), 1489–1506.
Trippanera, D., Ruch, J., Acocella, V., Rivalta, E., 2015. Experiments of dike-induced deformation: insights on the long-term evolution of divergent plate boundaries. J. Geophys. Res. Solid Earth 120 (10), 6913–6942.
Trippanera, D., Ruch, J., Acocella, V., Thordarson, T., Urbani, S., 2018. Interaction between central volcanoes and regional tectonics along divergent plate boundaries: Askja, Iceland. Bull. Volcanol. 80, 1–19.
Van Wijk, J.W., Blackman, D.K., 2005. Dynamics of continental rift propagation: the end-member modes. Earth Planet Sci. Lett. 229 (3–4), 247–258.
Walker, G.P., 1958. Geology of the Reydarfjördur area, eastern Iceland. Quart. J. Geol. Soc. 114 (1–4), 367–391.
Walker, G.P., 1960. Zeolite zones and dike distribution in relation to the structure of the basalts of eastern Iceland. J. Geol. 68 (5), 515–528.
Walker, G.P., 1965. Some Aspects of Quaternary Volcanism in Iceland. Leicester Literary and Philosophical Society.
Westoby, M.J., Brasington, J., Glasser, N.F., Hambrey, M.J., Reynolds, J.M., 2012. 'Structure-from-Motion' photogrammetry: a low-cost, effective tool for geoscience applications. Geomorphology 179, 300–314.
Wilson, D.S., Hey, R.N., 1995. History of rift propagation and magnetization intensity for the Cocos-Nazca spreading Center. J. Geophys. Res. Solid Earth 100 (B6), 10041–10056.
Wilson, J.T., 1963. Evidence from islands on the spreading of ocean floors. Nature 197 (4867), 536–538.
Xu, W., Jónsson, S., Corbi, F., Rivalta, E., 2016. Graben formation and dike arrest during the 2009 Harrat Lunayyir dike intrusion in Saudi Arabia: insights from InSAR, stress calculations and analog experiments. J. Geophys. Res. Solid Earth 121 (4), 2837–2851.
Zwaan, F., Schreurs, G., Rosenau, M., 2020. Rift propagation in rotational versus orthogonal extension: insights from 4D analogue models. J. Struct. Geol. 135, 103946.